

A practical model-based segmentation approach for improved activation detection in single-subject functional Magnetic Resonance Imaging studies

Wei-Chen Chen and Ranjan Maitra

Abstract—Functional Magnetic Resonance Imaging (fMRI) maps cerebral activation in response to stimuli but this activation is often difficult to detect, especially in low-signal contexts and single-subject studies. Accurate activation detection can be guided by the fact that very few voxels are, in reality, truly activated and that these voxels are spatially localized, but it is challenging to incorporate both these facts. We address these twin challenges to single-subject and low-signal fMRI by developing a computationally feasible and methodologically sound model-based approach, implemented in the R package MixfMRI, that bounds the *a priori* expected proportion of activated voxels while also incorporating spatial context. An added benefit of our methodology is the ability to distinguish voxels and regions having different intensities of activation. Our suggested approach is evaluated in realistic two- and three-dimensional simulation experiments as well as on multiple real-world datasets. Finally, the value of our suggested approach in low-signal and single-subject fMRI studies is illustrated on a sports imagination experiment that is often used to detect awareness and improve treatment in patients in persistent vegetative state (PVS). Our ability to reliably distinguish activation in this experiment potentially opens the door to the adoption of fMRI as a clinical tool for the improved treatment and therapy of PVS survivors and other patients.

Index Terms—Alternating Partial Expectation Conditional Maximization algorithm, Cluster thresholding, Expectation Gathering Maximization algorithm, False Discovery Rate, Flanker task MixfMRI, persistent vegetative state probabilistic threshold-free cluster enhancement, spatial mixture mode, traumatic brain injury

I. INTRODUCTION

Functional Magnetic Resonance Imaging (fMRI) is an imaging tool for understanding the spatial characteristics of human cognitive and motor function [1]–[6]. It is predicated on the significant discovery over three decades ago [7] that the firing of neurons in response to the application of a stimulus or the performance of a task is accompanied by changes in the blood oxygen levels in neighboring vessels, yielding the so-called Blood Oxygen Level Dependent (BOLD) contrast and that this BOLD effect is also present in human brains [8]. The BOLD effect causes a shift in the MR signal and is used in fMRI as a surrogate for neural activity. Images of BOLD measurements at each voxel – or volume element – are acquired at multiple times during or without the task- or stimulus-related activity and, before preprocessing to address the effects of motion and other artifacts, form the raw data from an fMRI experiment.

An important outcome of many fMRI experiments is the construction of voxel-wise maps to identify regions of neural activation. Such activation maps are often obtained by fitting a

general linear model [9] to the afore-mentioned raw data, that is, the BOLD time series observations at each voxel. Statistical Parametric Mapping [10] then reduces the data at each voxel to a test statistic that summarizes the association between the BOLD response and the stimulus time-course [3]. The test statistics (or their p -values) are thresholded to determine significantly activated voxels [11]–[14]. Many factors [15], [16] challenge detection accuracy, leading to much variation in identified activation from one study to another even when the same subject is scanned under the same paradigm [17]–[19]. Improving detection accuracy is important for clinical adoption of fMRI to understand and evaluate individual cognitive functions and to aid diagnosis by identifying pathologies.

There are many thresholding approaches to control the False Discovery Rate (FDR) [12], [20]–[22], with refinements [21] for weighted FDR to include spatial context and determine activation of clusters of voxels. Other approaches [23]–[26] use Random Field Theory and specified correlation structure on test statistics to calculate the threshold that produces an expected Euler characteristic [27] equal to the required p -value [11], [25]. Cluster-wise thresholding is perhaps the most popular approach and involves drawing clusters of a minimum number of connected voxels having p -values below a specified threshold [28], [29]. The method requires specification of neighborhood order, thresholding p -value and minimum cluster size. There has been little study on how neighborhood order impacts activation detection accuracy, but many researchers use a second-order neighborhood. Earlier p -value threshold recommendations [6], [30] of between 0.02 and 0.03 were deemed too liberal in [31] who suggested a more conservative default of 0.001. Threshold-free cluster enhancement (TFCE) methods [32]–[34] obviate the need for threshold choice but can have low spatial specificity for larger regions or need precise *a priori* information [31]. FDR in cluster-wise thresholding is controlled by choosing a minimum cluster size based on simulations under a null-activation model, but recent empirical studies have indicated cluster-wise thresholding implementations of popular fMRI software to have inflated false positive rates, both in single subject [35] and group [36] studies, though corrections and re-evaluation [36]–[38] have since indicated that the conclusion may have been unnecessarily alarmist.

The [39] highlighted the need for holistic approaches that account for the spatial, temporal and behavioral properties of the experiment and to improve SNR to make reliable inference at the single-subject level while also moving the field to

identify individual pathologies and help improve patient care in a clinical setting. In this context, [40] called for the linking of statistical methodology and the fMRI research paradigm to develop more accurate analysis methods, ensuring reliability and reproducibility.

One currently unexploited fact of fMRI activation studies is that only a very small [6], [33], [41] proportion (about 1-3%) of in-brain voxels are *a priori* expected to be truly activated. So, in this paper, we incorporate this information along with spatial context to improve detection accuracy even at the single-subject level in a computationally practical framework with the following objectives:

- Constrain *a priori*, the expected proportion of activated voxels. Importantly, this means *we do not strictly constrain the actual proportion of activated voxels in a particular study*, but rather, *we constrain the expected proportion of active voxels* to reflect our prior beliefs.
- Promote spatial contiguity and context in the detected activation so that activated voxels occur in clusters.

It is common to address the latter goal through the use of smoothing or through other devices such as a spatial mixture model [42], Markov Random Field priors such as the Ising model [43], [44], empirical Bayesian methods [45], [46] or Bayesian hierarchical modeling [47], [48]: however, these approaches have not been successfully coupled with our first objective that places a limit on the *a priori* expected proportion of activated voxels. Our approach postulates a mixture model for the distribution of the p -value of the test statistic at each voxel – the first mixture component represents the inactive voxels and has mixing proportion set to be no less than the *a priori* expected proportion of inactive voxels. Spatial contiguity in the detected activation is encouraged through a practical penalty term added to the loglikelihood function. Our showcase application, introduced in Section II, lays out the challenges in accurately detecting activation in a sports imagination experiment, illustrating both the need and value of our methodology because of its implications in moving fMRI to improve treatment and therapy of, for example, persistent vegetative state (PVS) patients.

The remainder of this paper is organized as follows. We provide practical methods for accurate activation detection in single-subject fMRI and discuss its implementation in Section III. We next comprehensively evaluate performance in simulation experiments in Section IV for a variety of levels and problem difficulty, in 2D, and different noise levels in 3D. We also evaluate performance on many standard datasets in the literature. Section V analyzes the sports imagination dataset introduced in Section II. The paper concludes with some discussion in Section VI. We also have appendices providing additional details on the preprocessing of our dataset, statistical methodology, experimental illustrations, performance evaluations, and data analysis.

II. IMPROVING TREATMENT OF PATIENTS IN PERSISTENT VEGETATIVE STATE VIA SPORTS IMAGINATION EXPERIMENTS

[49] reported that some PVS patients are known to retain some cognitive functions [50]. Indeed, the supplementary

motor area (SMA) was found to be significantly affected in the fMRI study [51] of a 25-year-old female Traumatic Brain Injury (TBI) survivor in PVS while she was verbally instructed to alternately rest and imagine playing tennis. Similar activation was observed in 12 healthy volunteers, so it has been surmised [51] and demonstrated [52] that fMRI can be used to diagnose conscious awareness and to communicate with PVS patients. A more elaborate study [53] found consistent activation (beyond the SMA, into the parietal cortex and other regions) in 14 normal subjects, but murky consistency in seven TBI patients. While healthy subjects necessarily have cognitive function that is mostly intact and regionally consistent in standardized (*e.g.*, Talaraich) space, TBI patients with injuries impacting brain structure and function may be missing some standardized regions, or show inconsistent disruptions across TBI-afflicted brains. It is therefore important that activation detection be reliable and accurate at the individual subject level, and achieving these goals is the rationale behind our proposed methodology.

We illustrate the challenges to accurate detection in single-subject fMRI experiments, by considering a healthy 40-year-old female volunteer [53] who was instructed to alternately rest or imagine playing tennis, in blocks of 30 seconds each, and with the entire 210-second study starting and ending with a resting block. [53] do not mention analysis of this dataset further, but the raw data were publicly released by [54] to demonstrate features of their **fmri** package in R [55]. We refer to Appendix A for details on data collection, preprocessing and analysis but note here that several methods, for example, after controlling for FDR at $q = 0.05$ [12], [56], permutation-based testing [57], thresholding by the value that produces an expected Euler characteristic [25], [27] equal to the desired p -value (taken to be 0.05 in this article), highlighting the challenges faced by global thresholding methods in accurately and reliably constructing activation maps in low-signal single-subject experiments. Such was also the result using spatial mixture modeling [42]. We also employed cluster-wise thresholding methods to detect activation, with the minimum number of contiguous voxels in each activated region determined using the 3dClustSim function of the Analysis of Functional Neuroimages (AFNI) software [58]–[60] at a threshold of 0.001 (following the recommendations of [31]) and using first-, second- and third-order neighborhoods. These three orders of neighborhood correspond to the definition of neighboring voxels accordingly as when their (1) faces, (2) faces or edges, and (3) faces, edges or corners touch. All three types of neighborhood found similar activated regions so we only display results (Fig. 1a) using a second-order neighborhood. The activation detected is mostly unemphatic. For instance, there is a very tiny blip of activation in the subject’s somatosensory cortex (left hemisphere) but not in her motor cortex or the SMA. The precuneus and the primary visual cortex are identified, but the extent of spatial activation (and clustering) is low. The diffidence in the described activation map could have led to misinterpretations (if we were not, for instance, aware of what we were expecting to be activated based on our prior knowledge of the activity or on the fact that we had a normal subject). It is important to note that in

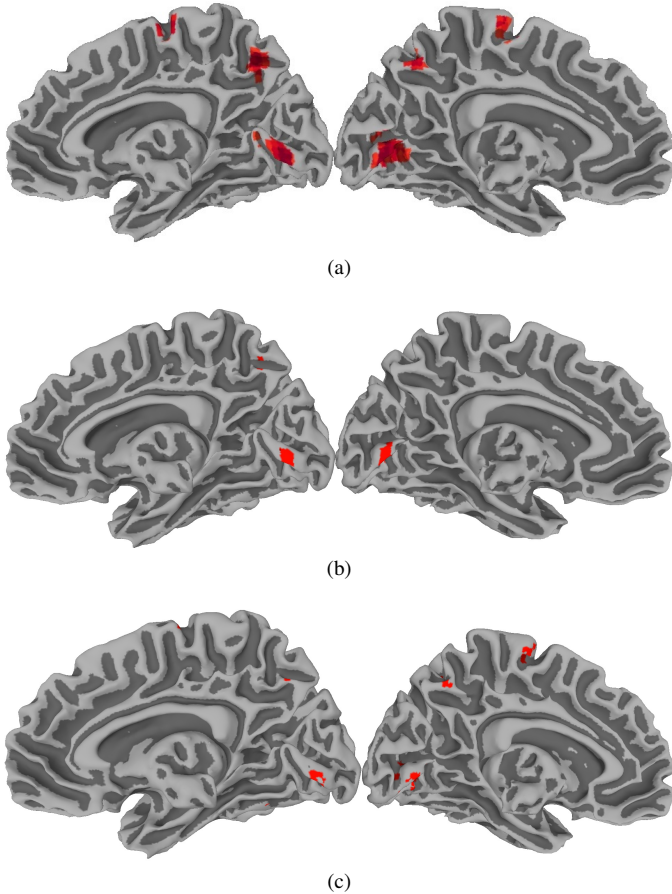


Fig. 1. Activation detected in healthy female volunteer performing a sports imagination experiment with (a) cluster-wise thresholding done using a second-order neighborhood, (b) pTFCE, and the (c) AR-FAST algorithm.

a clinical setting, where inference is desired at an individual subject level it is often not known beforehand (*e.g.*, a patient with a TBI) the particular regions of the brain that are expected to be activated.

Unclearer activation maps are obtained by probabilistic Threshold-Free Cluster Enhancement (pTFCE) [34] (Fig. 1b) – a refinement of Threshold-Free Cluster Enhancement (TFCE) [32] – or by the robust fast adaptive and smoothed thresholding (AR-FAST) method of [41] at $\alpha = 0.05$ (Fig. 1c). Activation is detected barely in the precuneus, or (with AR-FAST) the primary motor cortex (PMC). Other FAST methods [41] were also unsatisfactory.

This example indicates some of the challenges and inadequacies associated with the most common activation detection methods. For this normal subject, activation in the SMA is not easily detected by standard thresholding methods, despite the fact that several studies have found this region to be reliably activated in healthy subjects during sports imagination experiments. These deficits point to the need for improving activation detection methodology, and we explore doing so by incorporating the additional knowledge provided by both spatial context and prior belief on the expected proportion of activated voxels. These two ingredients are important and central to the application of activation detection in fMRI and have hitherto never been successfully incorporated into the

statistical methodology for analysis. It is the goal of this paper to redevelop such statistical analysis for the purpose of improving activation detection in fMRI. We revisit this dataset in Section V after developing our methodology.

III. METHODOLOGICAL DEVELOPMENT

Sections III-A–III-D build the framework and our methodology. The material can be highly technical, so we have provided a graphical overview in Section III-E for the reader who is most interested in a broad overview of our contributions.

A. Background and Preliminaries

Most current approaches to the statistical analysis of fMRI data involve post-hoc inference and analysis on obtained statistical parametric maps (SPMs). For instance, a popular approach to incorporating spatial context in activation detection is to use cluster-wise thresholding, or its derivatives, on the estimated p -values of test statistics obtained after fitting an appropriate model at each voxel. Another important aspect of fMRI activation, that is, the *a priori* known low expected proportion of active voxels is largely ignored. In this section, we address ways to formally incorporate these two features of fMRI activation in the statistical modeling and analysis.

As in most current software, we let $\mathbf{p} = (p_1, p_2, \dots, p_n)$ be the p -values of the test statistic at the n voxels in a fMRI volume, after fitting an appropriate model to test for activation in a first-stage analysis. We emphasize that this approach is marginally applied at each voxel for computational considerations, and also that the resulting statistics and their estimated p -values still maintain their dependencies that we account for shortly. Now, if the voxel-wise test statistic is known, for example, to be t -distributed, then each p_i can be modeled by an exact mixture model [19]. However, we instead build our method using an approximate but more general framework [61]–[63] that models each p_i as a mixture of the uniform (for the inactivated voxels) and beta distributions (for the different kinds, in terms of intensity of activation, of activated voxels). Let $b(\cdot; \alpha_k, \beta_k)$ be the beta density with shape parameters (α_k, β_k) . Then

$$p_i \sim f(p_i; \boldsymbol{\pi}, \boldsymbol{\alpha}, \boldsymbol{\beta}) = \pi_0 + \sum_{k=1}^K \pi_k b(p_i; \alpha_k, \beta_k). \quad (1)$$

with constraints:

- (i) $\boldsymbol{\pi} = (\pi_0, \pi_1, \dots, \pi_K)^\top$ lies on the K -dimensional simplex,
- (ii) $\pi_0 \geq \delta$ and
- (iii) $\alpha_k < 1 < \beta_k$ and $\alpha_k / (\alpha_k + \beta_k) \leq \eta \forall 1 \leq k \leq K$ with η the mean of the distribution of the p -value from an activated component.

From (ii), δ is the *a priori* expected minimum proportion of inactivated voxels while (iii) expresses that p_i s from activated components are expected to be declared significant.

The generative model for (1) stems from the distribution of the (observed) p -value at each voxel along with its (missing) class indicator. Let W_{ik} be 1 if the i th voxel is in the k th class ($k = 0, 1, \dots, K$) and 0 otherwise. Writing

$\boldsymbol{\alpha} = (\alpha_1, \alpha_2, \dots, \alpha_K)^\top$, $\boldsymbol{\beta} = (\beta_1, \beta_2, \dots, \beta_K)^\top$ and $\mathbf{W} = ((W_{ik}))_{1 \leq i \leq n, 0 \leq k \leq K}$, the complete log likelihood, assuming that the dependence in the \mathbf{p} s is through the generative \mathbf{W} s, is

$$\begin{aligned} \ell_c(\boldsymbol{\pi}, \boldsymbol{\alpha}, \boldsymbol{\beta}; \mathbf{W}, \mathbf{p}) &= \sum_{i=1}^n W_{i0} \log \pi_0 \\ &+ \sum_{i=1}^n \sum_{k=1}^K W_{ik} [\log \pi_k + \log b(p_i; \alpha_k, \beta_k)]. \end{aligned} \quad (2)$$

The Expectation-Maximization (EM) algorithm [64], [65] iteratively maximizes $\mathbb{E}[\ell_c(\boldsymbol{\pi}, \boldsymbol{\alpha}, \boldsymbol{\beta}; \mathbf{W}, \mathbf{p}) \mid \mathbf{p}]$ to yield maximum likelihood estimates (MLEs) of $(\boldsymbol{\pi}, \boldsymbol{\alpha}, \boldsymbol{\beta})$.

B. Incorporating spatial context

A shortcoming of (2), and thus of (1), is its disregard of spatial context. Modeling the W_{ik} s via a Markov Random Field (e.g. Potts' model) is computationally impractical because the expectation step (E-step) expressions are intractable, computed at each iteration only through time-consuming Markov Chain Monte Carlo (MCMC) or other methods. Our solution is to penalize (2) by adding the term

$$- \sum_{i \neq j=1}^n \sum_{k=0}^K W_{ik} W_{jk} \sum_{d=1}^3 \left[\frac{(v_{id} - v_{jd})^2}{h_{kd}^2} - \log h_{kd} \right], \quad (3)$$

with v_{id} s as the the i th voxel's coordinates in the 3D image volume (v_{i3} is omitted for 2D slices). For given k , (3) has the least effect when $W_{ik} W_{jk} = 1$ for nearby voxels i and j , and is like a regularization term in density estimation (but note that the v_{id} s are fixed here, while W_{ik} s are unobserved). The h_{kd}^2 s in the denominator modulate the influence of (3), varying by axes and with k to allow for localization. The additional $\log h_{kd}$ terms are for computational convenience (ensuring also that (3) is, but for a constant term of addition, a log density).

The terms for each axis (d) in (3) can be recast as

$$\sum_{i \neq j=1}^n \sum_{k=0}^K W_{ik} W_{jk} \frac{(v_{id} - v_{jd})^2}{h_{kd}^2} = \sum_{i=1}^n \sum_{k=0}^K W_{ik} \frac{(v_{id} - \mu_{kd})^2}{\sigma_{kd}^2}.$$

where we recast $\mu_{kd} \doteq \sum_{i=1}^n W_{ik} v_{id} / \sum_{i=1}^n W_{ik}$ and $\sigma_{kd}^2 \doteq h_{kd}^2 / 2$ for $d = 1, 2, 3$. The penalized complete log likelihood ((2) + (3)) is

$$\begin{aligned} &\sum_{i=1}^n \sum_{k=0}^K W_{ik} [\log \pi_k + \log b(p_i; \alpha_k, \beta_k) \\ &- \log |\boldsymbol{\Sigma}_k| / 2 - (\mathbf{v}_i - \boldsymbol{\mu}_k)^\top \boldsymbol{\Sigma}_k^{-1} (\mathbf{v}_i - \boldsymbol{\mu}_k) / 2] \end{aligned}$$

where $\alpha_0 = \beta_0 \equiv 1$, $\boldsymbol{\mu}_k = (\mu_{k1}, \mu_{k2}, \mu_{k3})^\top$, $\mathbf{v}_i = (v_{i1}, v_{i2}, v_{i3})^\top$ and $\boldsymbol{\Sigma}_k = \text{diag}(\sigma_{k1}^2, \sigma_{k2}^2, \sigma_{k3}^2)$. Maximizing (1) after incorporating the spatial penalty term is equivalent to maximizing $\ell(\boldsymbol{\Theta}; \mathbf{p}, \mathbf{v}) = \sum_{i=1}^n \log \left\{ \sum_{k=0}^K \pi_k f(p_i, \mathbf{v}_i; \boldsymbol{\Gamma}_k) \right\}$ with $f(p_i, \mathbf{v}_i; \boldsymbol{\Gamma}_k) = b(p_i; \alpha_k, \beta_k) \phi(\mathbf{v}_i; \boldsymbol{\mu}_k, \boldsymbol{\Sigma}_k)$, where $\boldsymbol{\Theta} = \{\boldsymbol{\Theta}_0, \boldsymbol{\Theta}_1, \dots, \boldsymbol{\Theta}_K\}$ with $\boldsymbol{\Theta}_k = \{\pi_k, \boldsymbol{\Gamma}_k\}$, $\boldsymbol{\Gamma}_k = \{\alpha_k, \beta_k, \boldsymbol{\mu}_k, \boldsymbol{\Sigma}_k\}$, $\phi(\mathbf{x}; \boldsymbol{\mu}, \boldsymbol{\Sigma})$ is the multivariate normal density with parameters $\boldsymbol{\mu}$, $\boldsymbol{\Sigma}$,

and $(\boldsymbol{\pi}, \boldsymbol{\alpha}, \boldsymbol{\beta})$ has the same constraints as (1) ($\alpha_0 = \beta_0 \equiv 1$ and do not have to be estimated). From an optimization perspective, this maximization is essentially equivalent to finding MLEs in a mixture model where each component $f(p_i, \mathbf{v}_i; \boldsymbol{\Gamma}_k)$ is the product of a beta density $b(p_i; \alpha_k, \beta_k)$ and a multivariate Gaussian density $\phi(\mathbf{v}_i; \boldsymbol{\mu}_k, \boldsymbol{\Sigma}_k)$ with diagonal $\boldsymbol{\Sigma}_k$ and mixing proportion π_k , for $k = 0, 1, \dots, K$. For a given K , the number of parameters to be estimated is $d_K = K(3 + 2c_v) + 2c_v$ with $c_v = 2$ or 3 for a 2D slice or 3D volume, respectively.

C. Parameter estimation and model-fitting

Adding (2) and (3) yields the penalized complete-data loglikelihood

$$\begin{aligned} &\sum_{i=1}^n \sum_{k=0}^K W_{ik} \left\{ \log \pi_k + \log b(p_i; \alpha_k, \beta_k) \right. \\ &\quad \left. - \frac{1}{2} \log |\boldsymbol{\Sigma}_k| - \frac{1}{2} (\mathbf{v}_i - \boldsymbol{\mu}_k)^\top \boldsymbol{\Sigma}_k^{-1} (\mathbf{v}_i - \boldsymbol{\mu}_k) \right\} \end{aligned} \quad (4)$$

while the penalized observed-data log likelihood equation is

$$\begin{aligned} \ell(\boldsymbol{\Theta}; \mathbf{p}, \mathbf{v}) &= \sum_{i=1}^n \log \left\{ \sum_{k=0}^K \pi_k f(p_i, \mathbf{v}_i; \boldsymbol{\Gamma}_k) \right\} \\ &\equiv \sum_{i=1}^n \log \left\{ \sum_{k=0}^K \pi_k b(p_i; \alpha_k, \beta_k) \phi(\mathbf{v}_i; \boldsymbol{\mu}_k, \boldsymbol{\Sigma}_k) \right\}. \end{aligned} \quad (5)$$

Development of a classical EM algorithm for parameter estimation given K is almost immediate, but the inseparability of (α_k, β_k) s from the beta function, the large scale of the problem with hundreds of thousands of voxels (in 3D), the need for constrained optimization and repeated initialization call for many refinements [66]–[69]. We develop strategies for parameter estimation and provide custom initialization schemes and a novel parallel Expectation-Gathering-Maximization (EGM) method for implementing the Alternating Partial Expectation Conditional Maximization (APECM) algorithm [70] through its APECMa variant [71].

1) Parameter estimation using the EM algorithm:

The classical EM algorithm has the E-step for calculating $w_{ik}^{(s+1)} = \mathbb{E}[W_{ik} \mid \mathbf{p}, \mathbf{v}, \boldsymbol{\Theta}^{(s)}] = \pi_k^{(s)} f(p_i, \mathbf{v}_i; \boldsymbol{\Gamma}_k^{(s)}) / \sum_{j=0}^K \pi_j^{(s)} f(p_i, \mathbf{v}_i; \boldsymbol{\Gamma}_j^{(s)})$ at the $(s+1)$ th iteration, with $\boldsymbol{\Theta}^{(s)}$ being the current value of $\boldsymbol{\Theta}$ obtained at the end of the s th iteration. At that iteration, the maximization step (M-step) maximizes

$$\begin{aligned} Q(\boldsymbol{\Theta}; \boldsymbol{\Theta}^{(s)}) &= \mathbb{E}[\ell_c(\boldsymbol{\Theta}, \mathbf{W} \mid \mathbf{p}, \mathbf{v}); \boldsymbol{\Theta}^{(s)}] \\ &= \sum_{i=1}^n \sum_{k=0}^K w_{ik}^{(s+1)} [\log \pi_k + \log f(p_i, \mathbf{v}_i; \boldsymbol{\Gamma}_k)] \end{aligned} \quad (6)$$

within the constraints (III-A), (III-A) and (III-A) that govern (1). The maximization of (6) is separable in $\boldsymbol{\mu}_k$ s, $\boldsymbol{\Sigma}_k$ s, $\boldsymbol{\pi}$ and $(\boldsymbol{\alpha}, \boldsymbol{\beta})$ and can be handled one subset of parameters

at a time. M-step updates for $\boldsymbol{\mu}_k$ and $\boldsymbol{\Sigma}_k$ are immediate, with $\hat{\boldsymbol{\mu}}_k^{(s+1)} = \sum_{i=1}^n w_{ik}^{(s+1)} \mathbf{v}_i / \sum_{i=1}^n w_{ik}^{(s+1)}$ and the (diagonal) matrix $\hat{\boldsymbol{\Sigma}}_k^{(s+1)}$ containing the diagonal elements of $\sum_{i=1}^n w_{ik}^{(s+1)} (\mathbf{v}_i - \hat{\boldsymbol{\mu}}_k^{(s+1)}) (\mathbf{v}_i - \hat{\boldsymbol{\mu}}_k^{(s+1)})^\top / \sum_{i=1}^n w_{ik}^{(s+1)}$. Updating $\boldsymbol{\pi}$ under constraints (III-A) and (III-A) requires some care however, so we state and prove the following

Result 1. Let $g(\boldsymbol{\pi}; \mathbf{W}) = \sum_{i=1}^n \sum_{k=0}^K w_{ik} \log \pi_k$, with $\boldsymbol{\pi} = (\pi_0, \pi_1, \dots, \pi_K)^\top$. Suppose that

- (a) $\boldsymbol{\pi}^*$ maximizes $g(\boldsymbol{\pi}; \mathbf{W})$ under the constraint that $h_e(\boldsymbol{\pi}) = \boldsymbol{\pi}^\top \mathbf{1} - 1 = 0$ where $\mathbf{1} = (1, 1, \dots, 1)^\top$ inside the convex set $\boldsymbol{\Pi} = \{\boldsymbol{\pi} : 0 \leq \pi_k \leq 1, k = 0, 1, \dots, K\}$.

Then, under the additional inequality constraint

- (b) $h_l(\boldsymbol{\pi}) = \pi_0 - \delta \geq 0$,

$g(\boldsymbol{\pi}; \mathbf{W})$ is maximized at $\pi_0^* = \max(\delta, \pi_0^*)$ and $\pi_k^* = (1 - \pi_0^*) \pi_k^* / (1 - \pi_0^*)$ for all $k = 1, 2, \dots, K$.

Proof. See Appendix B-A1. \square

Result 1 means that we can first ignore the inequality constraint (b) and estimate $\boldsymbol{\pi}$ only under the equality constraint (a) to get $\hat{\pi}_{k^*}^{(s+1)} = \sum_{i=1}^n w_{ik}^{(s+1)} / \sum_{k=0}^K \sum_{i=1}^n w_{ik}^{(s+1)}$. Then, if $\pi_0^{(s+1)} \geq \delta$, then $\hat{\pi}_k^{(s+1)} \equiv \hat{\pi}_{k^*}^{(s+1)}$ for all $k = 0, 1, \dots, K$. Otherwise, set $\hat{\pi}_0^{(s+1)} \equiv \delta$ and $\hat{\pi}_k^{(s+1)} = \frac{(1-\delta) \sum_{i=1}^n w_{ik}^{(s+1)}}{\sum_{k=1}^K \sum_{i=1}^n w_{ik}^{(s+1)}}$ for all $k = 1, 2, \dots, K$.

Since we do not have analytical expressions for M-step updates of $\boldsymbol{\alpha}$ and $\boldsymbol{\beta}$ within the constraints imposed by (iii), we use constrained optimization subject to linear inequality constraints and using an adaptive barrier, as in the `constrOptim()` function [66] in R [55]. Here also, (α_k, β_k) can be addressed separately for each $k = 1, 2, \dots, K$. The constrained optimization for α_k and β_k may not result in convergence at each M-step iteration owing to numerical issues. However, an increase in (6) is enough to guarantee convergence of the ML estimates for (5) as per the generalized EM algorithm [67]. Therefore, for $\boldsymbol{\alpha}$ and $\boldsymbol{\beta}$, we ensure an increased (6) within each M-step. We use the relative increase in the value of (5) over successive iterations $[\ell(\boldsymbol{\Theta}^{(s+1)}; \mathbf{p}, \mathbf{v}) - \ell(\boldsymbol{\Theta}^{(s)}; \mathbf{p}, \mathbf{v})] / [\ell(\boldsymbol{\Theta}^{(s)}; \mathbf{p}, \mathbf{v})] < \epsilon$ to determine convergence of our EM algorithms. In this paper, we set $\epsilon = 10^{-6}$.

2) *Initialization:* The EM algorithm only guarantees convergence to a local maximum with the initializing parameter values greatly influencing the converged ML estimates [72]. The need for effective initialization becomes more acute with increasing dimensionality and K [73]. Therefore, the choice of initial values is an important determinant in EM's performance. In order to increase the possibility of convergence to a global maximum, we modify the *Rnd-EM* approach of [72] to initialize $\boldsymbol{\Theta}^{(0)}$ in the presence of constraints. Exact specifics on the choice of the random initializing seeds are in Appendix B-A2.

3) *Parallelization of computations:* Despite its general wide appeal, the EM algorithm of Section III-C1 is plagued by slow convergence and can be time-consuming for typical 3D fMRI datasets with potentially upto a million voxels. While many speedup methods [65] exist, we incorporate the Alternating Partial Expectation Conditional Maximization (APECM, APECMa) algorithms of [70] and [71] that utilize

extra space to store and reduce calculations while being easily parallelizable on multi-core multi-processor computing architectures. Specifically, APECM and APECMa modify the Alternating Expectation Conditional Maximization (AECM) algorithm of [69] for mixture models by introducing a partial calculation of the E-step from the previous iteration (denoted as PE-step). This parsimonious computing yields faster EM convergence rates and shorter computing times. Further, data-distributed algorithms, such as the Expectation Gathering Maximization (EGM) algorithm [71] for distributed computing architectures can be coupled with APECM and APECMa to parallelize the M-step (really the conditional M- or CM-step) computations when local sufficient statistics are available. We refer to Appendix B-A3 for the exact details of our implementation of EGM with APECMa in our context.

4) *Choice of K :* Many methods (see e.g. [74]) exist for assessing K in a mixture model. The most popular are Akaike's An (AIC) [75] and Bayes (BIC) [76] Information Criteria (respectively, selecting K to be the one minimizing $\mathcal{B}_K = -2\ell(\hat{\boldsymbol{\Theta}}_K; \mathbf{p}, \mathbf{v}) + 2d_K$. Here $\hat{\boldsymbol{\Theta}}_K = \{(\hat{\pi}_k, \hat{\boldsymbol{\Gamma}}_k) : k = 0, 1, \dots, K\}$ contains MLEs of $\boldsymbol{\Theta}$ obtained for a given K , and d_K is the number of unrestricted parameters to be estimated in the model. Our approach to choosing K uses BIC, but additionally incorporates [77]'s suggestion that only reductions of BIC beyond 10 providing very strong evidence in favor of the more parameter-rich (larger- K) model. Formally, we choose the number of components as the first K for which $\mathcal{B}_K \leq \mathcal{B}_{K+1} + 10$, for $K = 0, 1, \dots, K_{\max} - 1$. We set $K = K_{\max}$ if no K satisfies this condition.

D. Merging of components and voxel classification

1) *Merging with inactive component:* Having determined K , we obtain an initial *maximum a posteriori* (MAP) classification of each voxel using the mixture model and estimated MLEs. Constraint (III-A) of (1) on the activated beta components ideally means that for $k > 0$, we get beta components with parameter estimates $(\hat{\alpha}_k, \hat{\beta}_k)$ $\hat{\alpha}_k / (\hat{\alpha}_k + \hat{\beta}_k) \leq \eta$. This last constraint on the expectation of the (activated) beta components logically follows from our expectation that these p -values are low for the activated components. We use $\eta = 0.05$ to match the most common threshold used in declaring an alternative hypothesis significant. However, the spatial penalty can also yield beta components with true mean $\alpha_k / (\alpha_k + \beta_k) \geq \eta$, because the spatial context does not involve the constraint (III-A) or the observed p -value. We merge such components with the inactivated (zeroeth) component via a hypothesis test of constraint (III-A). Specifically, for the k th ($k = 1, 2, \dots, K$) estimated beta component, we test $H_0 : \alpha_k / (\alpha_k + \beta_k) \geq \eta$ against $H_a : \alpha_k / (\alpha_k + \beta_k) < \eta$. We use the likelihood ratio test statistic (LRTS) $\Lambda_k = -2 \sum_{i=1}^{n_k} \{\log [b(p_{ki}; \hat{\alpha}_{0,k}, \hat{\beta}_{0,k})] - \log [b(p_{ki}; \hat{\alpha}_k, \hat{\beta}_k)]\}$ where n_k is the number of voxels classified to the k th component, p_{ki} s are the p -values of those voxels, $\hat{\alpha}_{0,k}$ and $\hat{\beta}_{0,k}$ are MLEs under H_0 and $\hat{\alpha}_k$ and $\hat{\beta}_k$ are MLEs under $H_0 \cup H_a$. The p -value of each of these K LRTSs is calculated using $\Lambda_k \sim \chi_1^2$, then converted to q -values to control for false discoveries [78]. Components for which we fail to reject H_0 are merged with the

inactivated component. We write \hat{K} as the number of activated comments remaining after these mergers.

2) *Merging of active components*: Similar to the case of inactivated components being possibly split into multiple groups because of spatial constraints, some of the remaining activated components are possibly identified as distinct only because they are spatially disjoint. We distinguish between spatially disjoint pairs of activated components with similar effect sizes from those that have distinct effect sizes. For each pair of activated components, we compared the parameters of the beta distributions representing the p -values of the components. Specifically, we tested the k th and l th activated component means using $H_0 : (\alpha_k, \beta_k) = (\alpha_l, \beta_l)$ against the alternative $H_a : (\alpha_k, \beta_k) \neq (\alpha_l, \beta_l)$ using a LRTS which is given by $\Lambda_{kl} = \sum_{i=1}^{n_k} \{\log \{b(p_{ki}; \hat{\alpha}_{kl}, \hat{\beta}_{kl})\} + \sum_{i=1}^{n_l} \log \{b(p_{li}; \hat{\alpha}_{kl}, \hat{\beta}_{kl})\} - \sum_{i=1}^{n_k} \log \{b(p_{ki}; \hat{\alpha}_k, \hat{\beta}_k)\} - \sum_{i=1}^{n_l} \log \{b(p_{li}; \hat{\alpha}_l, \hat{\beta}_l)\}$ where $p_{ri}, i = 1, 2, \dots, n_r$ is the set of p -values at the n_r voxels classified to the r th component, $r \in \{k, l\}$, $(\hat{\alpha}_r, \hat{\beta}_r)$ is the MLE of (α_r, β_r) obtained from fitting a beta distribution to the p -values classified to the r th component, and α_{kl}, β_{kl} are the parameter MLEs obtained upon fitting a beta distribution to the combined sample of p -values. Under the null hypothesis, the asymptotic distribution of $-2\text{LRTS} \sim \chi_2^2$. To account for the $\binom{\hat{K}}{2}$ pairwise tests, we used q -values [78] larger than 0.05 to merge pairs of spatially separated active clusters with indistinguishable beta distribution parameters.

3) *Voxel classification*: Voxels are initially classified into the initial \hat{K} groups in terms of the highest MAP. After the potential mergers of Section III-D, the voxels in the merged groups provide a final classification of each voxel as inactivated or activated (in one of the merged, activated groups). The (merged) activated groups represent activated voxels of different intensities and correspond to different strengths of activation.

E. Overview of our methodology

Figure 2 provides a flowchart of all the steps in our methodology. The starting point is the map of voxel-wise p -values of a SPM obtained from some standard fMRI processing software. Each p -value is modeled by a mixture density, as in (1). To the loglikelihood model derived from these mixture densities, we add penalties for spatial context and constraints for the maximum *a priori* expected proportion of activated voxels, as detailed in Sections III-A and III-B. We then use the development in Section III-C to estimate the parameters of the beta mixture model, and the number of mixture components (using BIC). Each voxel is classified to the mixture component having the highest posterior probability. The components are then merged, per the results of hypothesis tests, following the development of Section III-D.

F. Extension to a two-sided testing framework

Our methodology is easily extended to situations involving two-sided p -values. In this situation, we consider the two one-sided p -values (for the left and right tail) individually, and run our methodology, with δ replaced in each case by δ_l and δ_r ,

depending on the practitioner's minimum *a priori* expected proportion of inactive voxels in the right and left tail. If the practitioner can only provide an overall minimum *a priori* expected proportion of inactive voxels (δ), then we suggest using $\delta_l = \delta_r = 1 - (1 - \delta)/2$. We illustrate and evaluate performance using the above methodology on 26 Flanker task datasets in Section IV-B3.

In this section, we have developed and fine-tuned statistical methodology for application to detecting activation in fMRI studies. We now evaluate its performance in realistic simulation experiments before applying it to our sports imagination experiment dataset.

IV. PERFORMANCE EVALUATIONS

We very comprehensively evaluated our activation detection methodology. Our evaluation setups included simulation experiments in realistic 2D and 3D settings, and on 81 real datasets from four different task paradigms. The performance of our activation detection methodology (denoted as MixfMRI or Mf in our figures) was compared with a host of commonly used alternatives, that either have software available or are easily coded, and, because our evaluations are over hundreds of simulated and real datasets, are computationally practical to use, implement and evaluate. Consequently, we do not include comparisons with Bayesian methods, such as those in [44] that use computationally expensive MCMC methods and were demonstrated only in 2D, and for which code is unavailable. Our comparisons only use the enhanced versions of methods if the improvements have been shown to improve activation detection: for instance, we use pTFCE instead of TFCE [34], and the fully-automated FAST methods [41] instead of structural adaptive segmentation [79]. An added benefit here is the ready availability of software for both pTFCE and FAST (while the R package **fmri** implements structural adaptive segmentation, the software when applied to our datasets threw up errors that were not resolved even after communicating with the authors). We note also that [41] showed poorer performance of both TFCE [32] and adaptive segmentation [79] in their extensive simulation and real data experiments. Therefore, for comparison, we use (a) thresholding, after controlling for false discoveries [56] at 0.05 (abbreviated as FDR in our figures), (b) thresholding computed by using Random Field theory (abbreviated using RF) to get a specified p -value of 0.05 [25], (c) cluster-based thresholding with a first-order (CT-1st), second-order (CT-2nd) or (and in the case of 3D) third-order (CT-3rd) neighborhoods, all with cluster sizes decided by AFNI and a thresholded p -value of 0.001, following [31], (d) the three sets of FAST methods [41] with parameter $\alpha = 0.01$ or 0.05: AM-FAST (AM, $\alpha = 0.01$ or AM, $\alpha = 0.05$ in our figures, AR-FAST (AR, $\alpha = 0.01$ or AR, $\alpha = 0.05$), and ALL-FAST (ALL, $\alpha = 0.01$ or ALL, $\alpha = 0.05$), (e) permutation testing at $\alpha = 0.05$ ("Permutation" in our figures), and (f) the spatial mixture model method (or SMM in our figures), of [42]. We also evaluated performance, in the case of our 2D experiments, using our methodology that included the proportion-of-inactives ($\pi_0 \geq \delta$) constraint, but not the spatial constraint (denoted as MfnoX in our figures). Therefore,

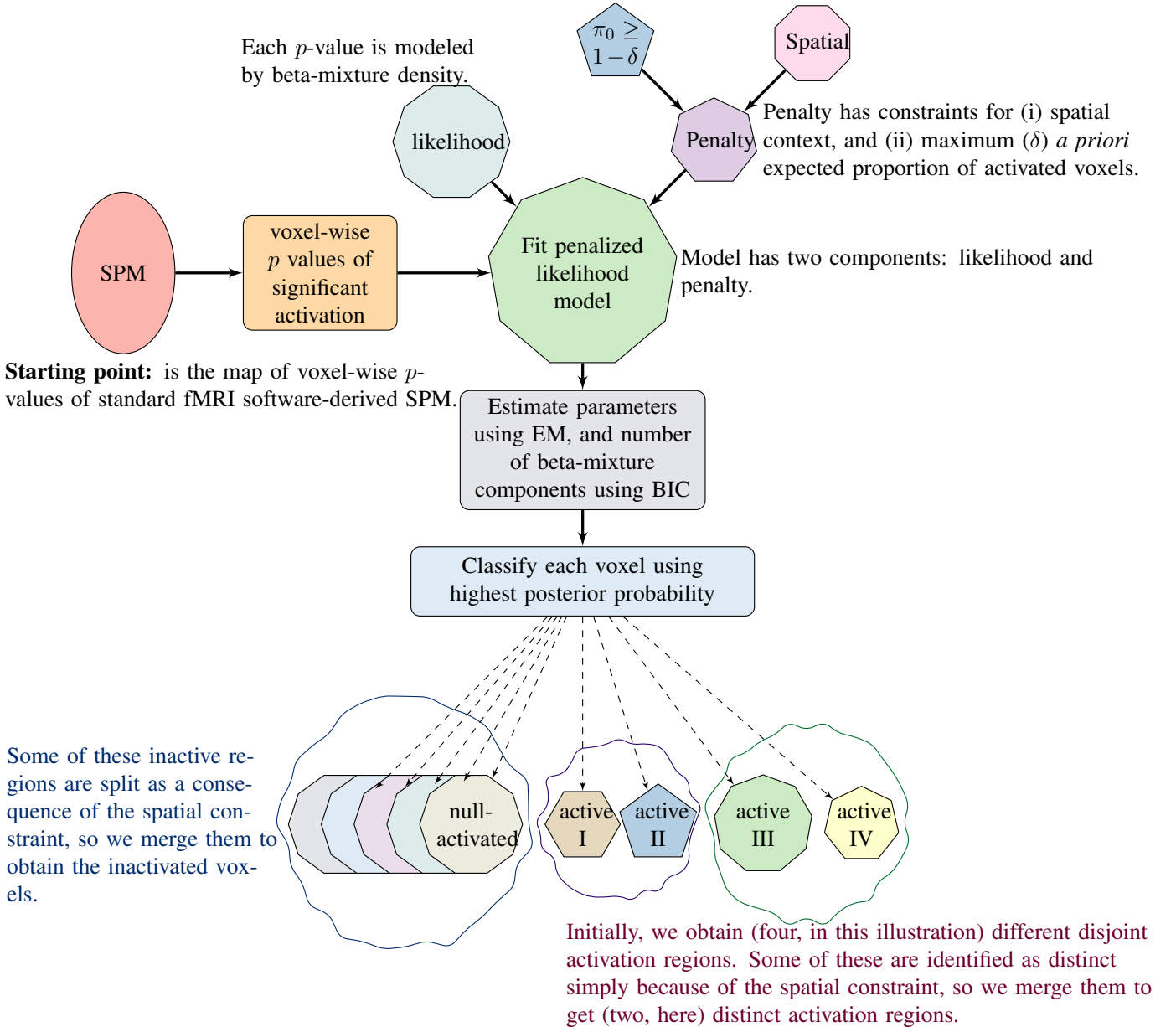


Fig. 2. Graphical illustration of our modeling, estimation and algorithmic framework. Abbreviations used: SPM, Statistical Parametric Map; EM, Expectation Maximization algorithm; BIC: Bayesian Information Criterion.

including the methodology developed here, and with different specifications of δ , our comparisons are over a total of 19 methods. Our methodology, with or without spatial constraints, was applied using our R package **MixfMRI** [80], while we used our coded R scripts for FDR and permutation testing. The R package **AnalyzefMRI** [81] was used for RF, cluster-wise thresholding and spatial mixture modeling, while we used **pTFCE** [34] for pTFCE, and **RFASTfMRI** [41] for the FAST methods. For all methods, activation detection accuracy was numerically assessed by the Jaccard index \mathcal{J} [82], [83] that is the ratio of the number of voxels that are both identified as active and truly so and the number of voxels that are either truly active, so detected or both. The index \mathcal{J} takes values in $[0,1]$, with 0 indicating that no voxels are correctly identified as activated and 1 indicating perfect detection. Finally, we

evaluated the unique ability of MixfMRI to detect the different kinds of activation by calculating the adjusted Rand index [84] between our estimated activation maps and the ground truth in our simulation experiments. This index, or ARI, takes values in $(-\infty, 1]$ with the upper limit indicating perfect predicted classification, and values farther away from 1 signifying poorer agreement of the classification with the truth. The ARI is expected to be zero when the voxels have been randomly classified.

A. Simulation Experiments

1) Two-dimensional framework:

a) *Experimental setup:* We evaluated our methodology on digitized 2D phantom [85], [86] datasets commonly used in Positron Emission Tomography experiments and specifically

redesigned by us to mimic p -values typically obtained in fMRI experiments. Our setup is in 2D to permit a very thorough and detailed large-scale analysis, while also being realistic enough to capture the challenges in 3D settings. Our phantom (Figure 3) had different-sized and oriented digitized ellipses, each representing hypothesized structures in the brain with some of them presumed activated by stimulation. We considered three scenarios. The first case (Figure 3a) had very little (0.9% of all

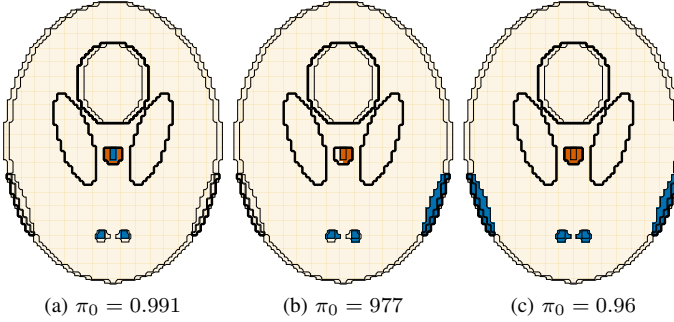


Fig. 3. The phantom with three areas of simulated activation (in darker colors) that was used in our experiments. (The two dark colors indicate the two different intensities of activation.) In (a), the phantom has very few areas of true activation while in case (b), the phantom shows activation only on one side (and with smaller spatial extent) while in (c) the phantom shows activation that is bilateral (on both sides).

“in-brain” pixels) true activation. The second case (Figure 3b) had 2.3% truly activated in-brain pixels, with all activation on one side of the brain, as would happen, say, in a one-hand finger-tapping experiment. The third case (Figure 3c) had 3.97% of truly activated in-brain pixels with activation that is symmetric on both sides (as expected, say, in a bilateral finger-tapping experiment.) In each case, two regions (shown in darker colors) of differing strength are truly activated. Thus, the true π is (0.991, 0.005, 0.004), (0.977, 0.019, 0.004) or (0.96, 0.034, 0.006) for the scenarios in Figure 3. For all cases, $K = 2$ is the number of active components when ignoring spatial context. However the activated components span multiple homogeneous spatial regions. Ignoring spatial context, each of the two activated components corresponds to one of the two non-uniformly distributed components of our generative mixture model whose choice we now discuss.

For simulating the p -values for our experiments, we forewent the beta distributions for the p -values of the activated regions, and instead chose the distribution of the p -value of a one-sided normal test statistic: $\psi(p; \nu_k) = \phi(\Phi_z^{-1}(1-p); \nu_k, 1) / \phi_z(\Phi_z^{-1}(1-p))$, where $\Phi_z(\cdot)$ and $\phi_z(\cdot)$ are the standard normal distribution and density functions, and $\phi(\cdot; \nu_k, 1)$ is the normal density function with mean ν_k and variance 1. (For inactivated pixels, $\nu_0 = 0$ and $\psi(p; \nu_0)$ is the uniform density. We reiterate that $\psi(p; \nu_1)$ and $\psi(p; \nu_2)$ are the densities corresponding to the two activated components in our generative model.) We use $\psi(p; \nu_k)$ s rather than $b(p; \alpha_k, \beta_k)$ s in simulating our datasets in order to gauge performance when the p -value mixture distributions are only approximately modeled by (1). Therefore, our choice of simulation model does not match the model on which our estimation methodology and software are built, but as a result, provides us more real-

world performance assessments. Note also that RF, the FAST methods, pTFCE and spatial mixture modeling are meant for use on Gaussian SPMs, so the generative model may be considered to be somewhat more favorable for their frameworks. For these methods which detect activation using SPMs, we converted each of our simulated p -values to the corresponding upper standard normal quantile before application.

We performed experiments in scenarios ranging from easy (typical in low-level, easily-differentiated motor task experiments) to difficult activation detection scenarios (as in higher-level tasks requiring finer levels of cerebral processing). We obtained these scenarios by relating the values of $\nu_0 \equiv 0$, ν_1 and ν_2 to the pairwise overlap measure ω [73] calculated between the unique pairs of densities characterized by $\{\nu_0, \nu_1, \nu_2\}$. Specifically, given $\nu_0 = 0$ and for each of the π s in Figure 3, we chose (ν_1, ν_2) such that the overlap between every pair of the three mixture components was set to be ω for $\omega \in \Omega = \{0.01, 0.1, 0.25, 0.5, 0.75, 0.95\}$. Thus, our simulated mixtures had components ranging from mildly well-separated ($\omega = 0.01$) to essentially indistinguishable ($\omega = 0.95$). We call ω the *identification complexity parameter* and regard it as a surrogate for the difficulty of the particular activation detection problem, with higher values reflecting greater difficulty in detecting activation. Figures 14, 15, and 16 display sample mixture distributions and simulated statistical parametric maps (SPMs) for three ω s, and for each of the three phantoms. These SPMs were obtained from our simulated datasets by using the inverse standard Gaussian cumulative distribution function on the simulated p -values at each voxel.

We simulated 25 datasets at each $\omega \in \Omega$ for each phantom, and obtained activation maps using our APECMa-EGM algorithms and its competitors. Recognizing that a practitioner may not (be able to) specify δ with complete accuracy, we evaluated performance of our method, and its counterpart that ignored the spatial penalty, with $\delta \in \{0.95, 0.975, 0.99\}$ to evaluate sensitivity of our results to such potential δ -misspecification. For all experiments, we set $K_{\max} = 8$.

b) *Simulation results:* We now detail and discuss our results.

Sample illustrations: Figure 4 illustrates activation detected using our method on sample realizations (see Figures 14, 15 and 16) of each of the phantoms in Figure 3, and with identification complexity parameter (ω) ranging from the easy ($\omega = 0.01$) to the substantially ($\omega = 0.5$) to very difficult ($\omega = 0.75$). Figure 14 also has activation detected using (where applicable, the best-performer among) the other methods for the simulated dataset corresponding to Figure 3a, while Figures 15 and 16 have the corresponding results for Figures 3b and 3c. (AM-FAST generally does poorly in many of these cases, so is excluded in these individual displays for compactness.) Our approach is generally a top performer in each of the examples, and this better performance is sustained even with increasing activation detection difficulty (ω). However, in these examples, the SMM of [42] is often the best performer. Cluster thresholding (CT-2nd or CT-1st, that is not shown), and FDR also do excellently, but under very low ω . With very localized true activation (corresponding to the phantom in Figure 3a), ALL-FAST does relatively well even

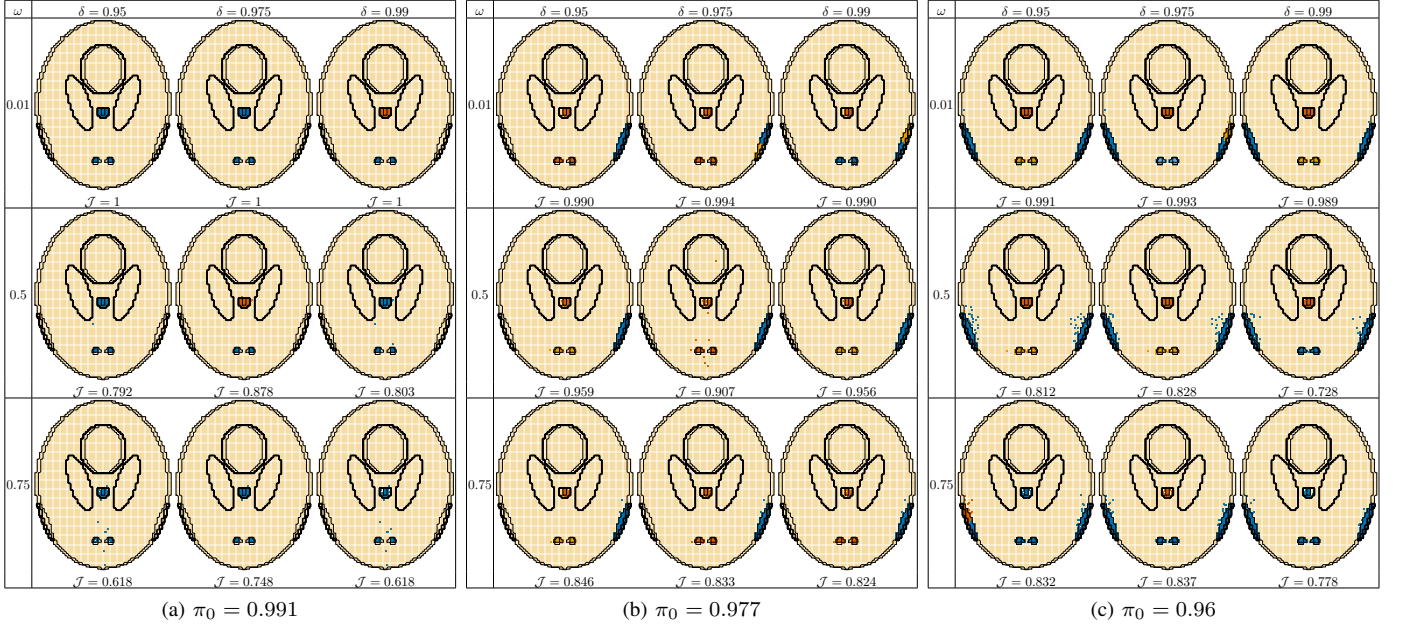


Fig. 4. Activation obtained using our method on sample realizations obtained using different ω for the three phantoms in Figure 3.

when ω increases (Figure 14). For the other phantoms, pTFCE also does relatively well with low ω , but only SMM, ALL-FAST and AR-FAST are competitive with higher identification complexity. Despite the good \mathcal{J} s, we see that the FAST methods overestimate the spatial extent of activation. Permutation-testing is a poor performer across the board, in these examples. In general, many of the alternative methods degrade quicker in performance than our method. Further, setting only the δ constraint provides good performance, but not always, and in any case, the improvement is not as much as that obtained when also including the spatial penalty. Finally, the unique ability of our methodology to potentially detect the different kinds of activation shows some promise. The results displayed here are on one candidate realization at the sample settings, so we now report performance of all the methods in our large, comprehensive simulation study.

Comprehensive evaluations: Figure 5 summarizes the ability of MixfMRI to identify the different intensities of activation, for $\delta \in \{0.95, 0.975, 0.99\}$. We see that while there is degradation in this ability with increasing identification complexity, the performance is very good at lower ω s. Indeed, but for the phantom (with $\pi_0 = 0.991$) having very little true activation, the ARI is quite high even for ω as high as 0.75. Thus, the performance of MixfMRI in recovering the different kinds of activation is encouraging. Most other methods do not have this ability, mostly providing only a binary classification of each voxel as activated or not, so we now evaluate all the methods in terms of \mathcal{J} .

Figure 6 summarizes the results of all the two-dimensional simulation experiments, with Figure 6a displaying the performance of all methods on the three phantoms and under different ω s through the \mathcal{J} s. Figure 6b provides the q -value [78] of the paired Wilcoxon signed rank test for whether the \mathcal{J} s obtained by MixfMRI with a given δ is different from any of

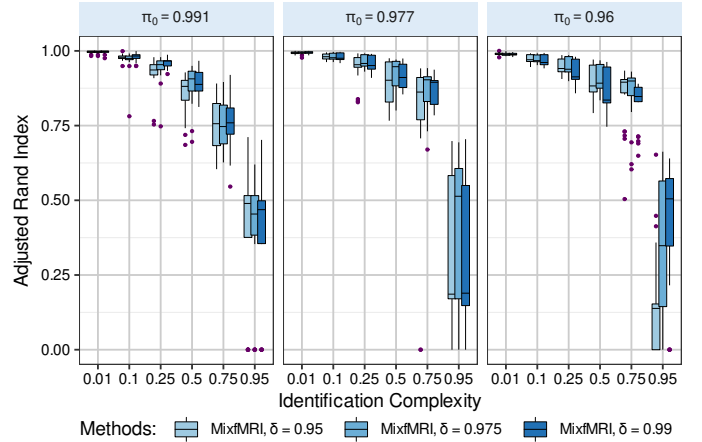
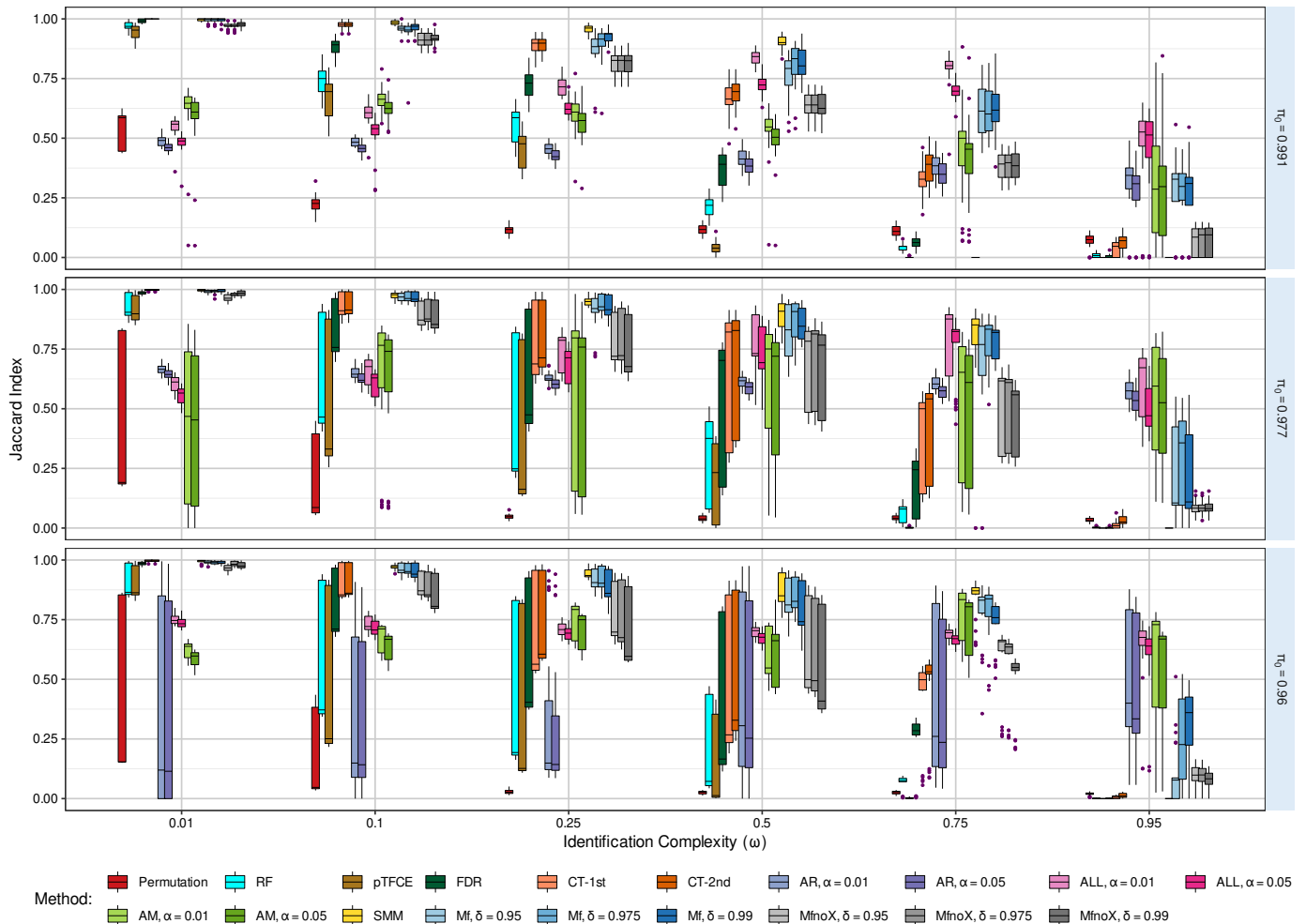
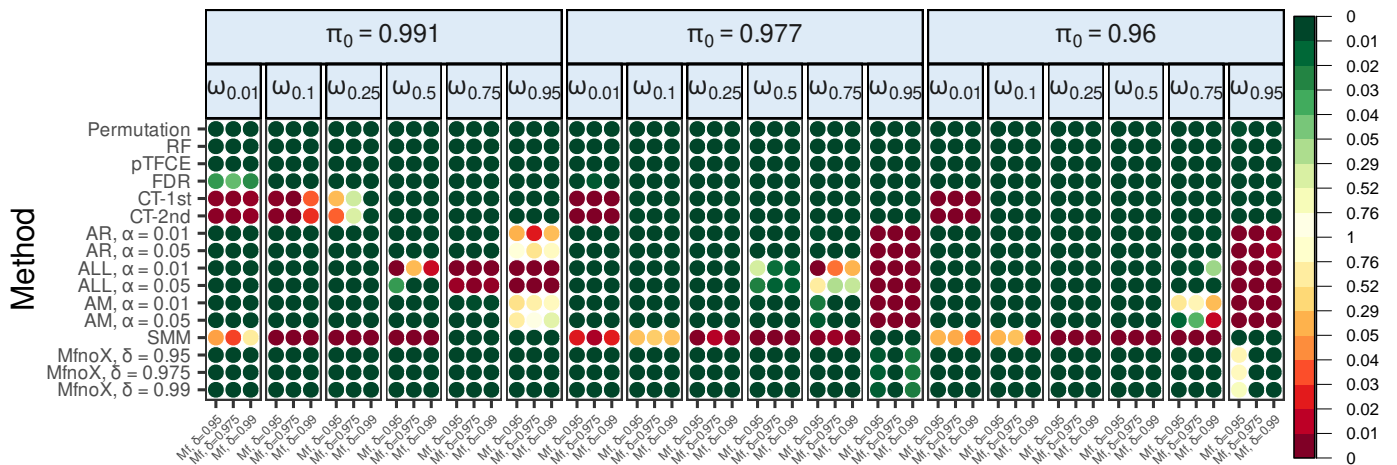


Fig. 5. The adjusted Rand index summarizing our method’s ability to identify the different kinds of activation in each phantom for each δ and ω .

the competing methods. (The display differentiates between when MixfMRI is better or worse, and shows that we are significantly better (dark greens) than the competitor in most cases.) For easy problems ($\omega = 0.01$), Figure 6a repeats the trends shown in Figure 4, and does not show much important distinction between our methodology and the best-performers such as CT-1st or CT-2nd (which report near-perfect \mathcal{J} s), or the spatial mixture model, even though many of these differences are statistically significant (Figure 6b). The FAST methods are generally substantially inferior at these low ω s and continue to perform indifferently for moderate ω , but they, and in particular ALL-FAST, perform very well for higher ω and with very small amounts of activation (the phantom of Figure 3a). Interestingly, [41] suggested using $\alpha = 0.01$ and $\alpha = 0.05$ for low- and high-noise situations, but in these experiments, the FAST methods with $\alpha = 0.01$ generally had



(a) The Jaccard index summarizing results of all methods on all replicates in our 2D simulation experiments. The row panel indicates the phantoms (indexed by the true π_0). Each group of boxplots corresponds to a given identification complexity (ω), with the methods in each group in the same order as the labels in the figure.



(b) The q -value obtained from the two-sided paired Wilcoxon signed rank test of the \mathcal{I} s obtained using our method (on the horizontal axis, for a given δ) and each competitor (on the y axis) for each phantom and experimental setting (here ω_α denotes identification complexity of α). In all cases, darker values indicate significant differences between the competing methods. The yellow-to-green map displays the q -value for the cases when our method is better than a given competitor for a specific experimental setting, while the yellow-to-red map displays the q -value for the cases where our method is worse. (The q -value scale in our display is piecewise linear, with a steeper gradient in $[0,0.05]$ than in $[0.05,1]$).

Fig. 6. Comprehensive summary of the results of our 2D simulation experiments. The methods are in the same order in both figures and use the abbreviations outlined at the beginning of Section IV.

higher \mathcal{J} s than those obtained using $\alpha = 0.05$. While all other methods degrade with increasing identification complexity, our method performs better relative to the alternatives. Even with $\omega = 0.75$, the median \mathcal{J} was very good for our methods, though there was greater variability in performance. The spatial mixture model approach was the best performer in these 2D experiments in all but for the highest ω (and in many cases, significantly better than our methods). As in the case of the single realization case earlier, permutation testing was the worst performer across all ω s and phantoms. Finally, including the spatial penalty in our method improves performance over our method implemented without the spatial penalty, so for concision and ease of presentation, we drop displays and discussion on the case that only involves the proportion-of-inactive-voxels constraint and not the spatial penalty.

Our comprehensive evaluations on 2D simulated single-subject scenarios show competitive performance of our methodology that incorporates both *a priori* expected proportion of activated voxels and spatial context. Our methodology is robust and a good performer even under high identification complexity, which portends well for its use in experiments involving high-level cognitive tasks, as in the case of our showcase application. Additionally, as seen in Figures 4 and 5, we can identify the different intensities of activation fairly well. We now evaluate performance in realistic 3D simulation settings.

2) *Three-dimensional framework*: Our 3D simulation experiments used the **neuRosim** [87] R package that simulates time series fMRI data according to a desired experimental paradigm. We used the simulation setup presented in [87] that mimics the real-life repetition priming experiment of [88], with the exception that the radii of the five activated regions on Page 12 of [87] were each decremented by one to match a more realistic proportion (2.74%) of in-brain activated voxels (and that in the real-life study in [88]). We used four different SNRs of 0.9925, 1.785, 3.87, and 7.74 to characterize varying levels of noise that can impact activation detection ability. Our evaluation was on the SPM formed by the faces-versus-baseline contrast, with the SPM converted to a p -value map where needed, such as for our methods. For each SNR, we simulated 25 four-dimensional fMRI time series datasets, and obtained the corresponding 25 SPMs and p -value maps. Activation was detected using our method (with $K_{\max} = 11$) and its competitors. Figure 7 shows that the ARIs are modest under very low noise, and quite high in all other cases, indicating good ability of our method in determining the different kinds of activation. Figure 8a displays the \mathcal{J} s obtained using our method and its competitors, with the significance of the differences between our method and its competitors summarized in Figure 8b. The ALL-FAST methods are the best performers among the competitors (and in a few cases even significantly better than our methods for the lowest SNR), but not significantly different (even if slightly worse) than our methods for moderately low SNR. Also, SMM is worse, but not significantly so, than our method for very low SNR. Further, while pTFCE is significantly better than our method at the highest SNR level, Figure 8a indicates that this difference in performance may not be significant. Against all

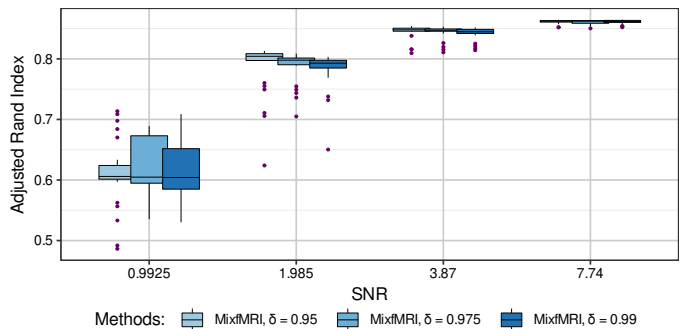


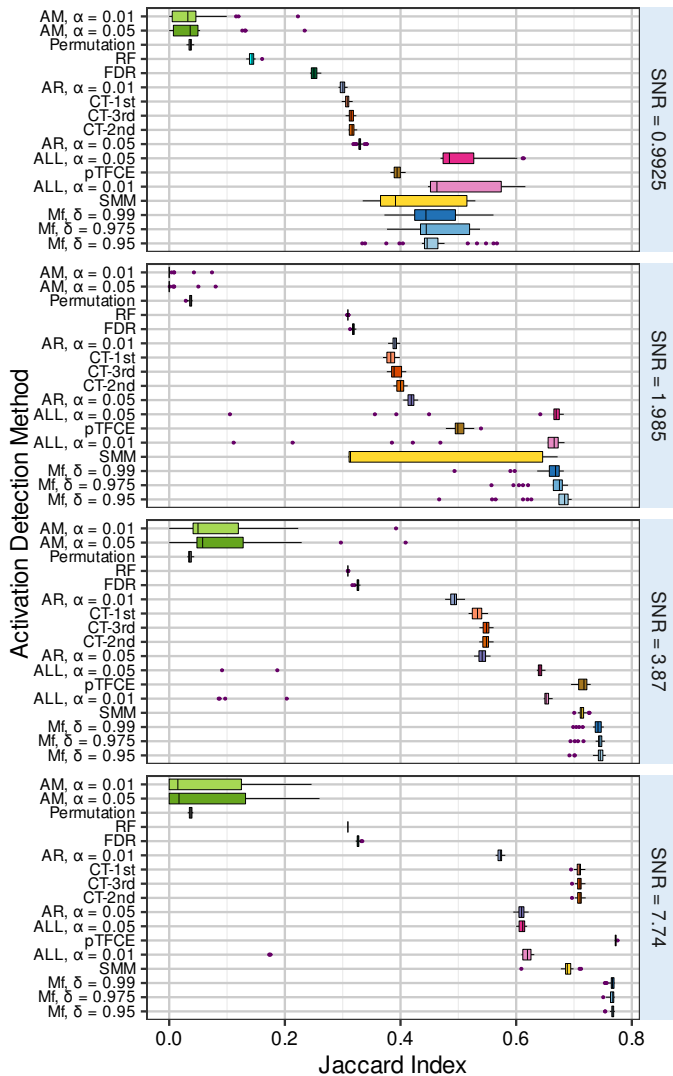
Fig. 7. The adjusted Rand index summarizing our method’s ability to identify the different kinds of activation at each SNR, for different δ .

other methods, our method is a substantially better performer, and significantly so. AM-FAST and permutation testing are the worst performers at all SNRs. An interesting observation is the poorer performance of SMM than in the 2D simulation studies earlier.

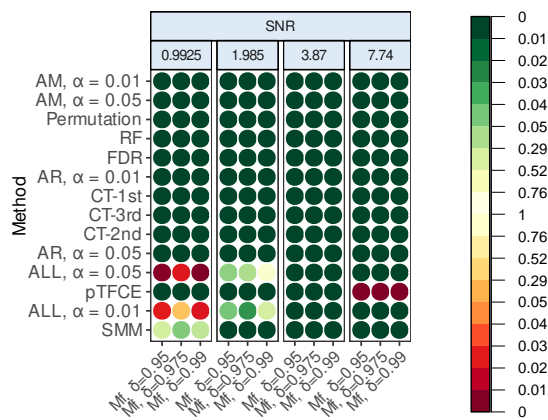
Our experiments show good performance of our methodology for a large range of realistic 2D and 3D simulation experiments. In some cases, we are bettered by the competitors, with, and especially in 3D settings, the differences being sometimes significant but not always important. On the other hand, we are better in most cases, and in many of these cases the differences are both significant and substantial enough to be important. Our methodology is also seen to do fairly well in detecting the different kinds of activation. We now evaluate performance of the method and its competitors over some real data examples.

B. Performance on Real Data Examples

Our next tranche of evaluations is on 81 datasets from three sets of fMRI studies. We first evaluated the performance of our algorithm in null activation resting state scenarios for each of 31 typically developing children [89]. The second set of experiments was from the right- and left-hand finger-tapping study [17], [41], [72], [83] of a normal male volunteer over 12 sessions spanning two months. The final set of experiments were from a Flanker experiment [90] on 26 right-handed adults. For all but the spatial mixture model and the FAST methods, we spatially smoothed the SPMs obtained in each of the experiments using the automated robust method of [91] that uses the generalized cross-validation to adaptively estimate the smoothing parameter. These smoothed maps were used to obtain the p -value maps of activation or significance at each voxel. We do not apply smoothing to the SPM for the FAST methods where smoothing is an integral part of the adaptive smoothing and thresholding algorithm. Similarly, [42] also express concerns about smoothing of the SPM before activation detection, and so we report on their results obtained without prior smoothing. (Each of these methods were also seen to perform better without prior smoothing of the SPM, while the other methods performed better with the prior smoothing of the SPM.) Further, there is no ground truth available for the finger-tapping and the Flanker task experiments,



(a) The Jaccard index of all the methods evaluated on 25 SPMs obtained from fMRI time series data simulated using **neuRosim**, under different SNR. Methods are listed in increasing order of their overall median \mathcal{J} .



(b) The q -value of the two-sided paired Wilcoxon signed rank test of the \mathcal{J} obtained using our method (horizontal axis) at a given δ and each competitor (in the same order as in Figure 8a). Displays and scales are as in Figure 6b.

Fig. 8. Comprehensive summary of our 3D simulation experiments.

so for each experiment, we used the summarized Jaccard index (\mathcal{J}) of [83] to measure consistency in the activation identified between the different replicates. The summarized Jaccard index, proposed by [83] for evaluating consistency in several activation maps, first constructs a matrix Ω of the Jaccard index between every pair of activation maps and then calculates \mathcal{J} over all the (M) activation maps in terms of its largest eigenvalue $\omega_{(1)}$. Formally, $\mathcal{J} = (\omega_{(1)} - 1)/(M - 1)$. It is easy to see [83] that $0 \leq \mathcal{J} \leq 1$ with $\mathcal{J} = 0$ when there is no agreement at all between any of the maps, because then Ω is an identity matrix. Further, $\mathcal{J} = 1$ when all the activation maps are in complete agreement with each other. We now describe and discuss the results in each experimental study.

1) *Resting state datasets*: The data used in this set of experiments are from the resting state fMRI scans of 31 typically developing adolescent children that were acquired using a single-shot, parallel (SENSE) gradient-recalled echo planar sequence (TR = 2500 ms, TE = 30 ms, and a flip angle of 70°) over 156 time points, with the image volumes at each time-point having axial slices of 3mm each and no slice gap. We used AFNI [58]–[60] to pre-process the dataset and then fit a general linear model with autoregressive errors for a purported auditory experiment to the data. The SPMs obtained from each dataset, and their associated p -values were then submitted to our methodology ($K_{\max} = 11$) and its competitors to obtain activation maps. Figure 9 provides a heatmap of the proportion of voxels identified in each dataset (indexed by its unique seven-digit identifier) as activated by each method. (For our method, we only report performance with $\delta = 0.95$ since our results obtained using other values of δ were identical.) No activation was detected, correctly, using our methodology, RF, pTFCE, cluster thresholding, or FDR. The spatial mixture model approach correctly found no activation in 30 of the datasets, but also was unable to provide a solution for the remaining dataset. The FAST methods find varying amounts of activation in at least some of the SPMs, while permutation testing detected a very small proportion of active voxels in every dataset. [36] has stressed the importance of evaluating the false positive rate of activation detection algorithms on resting state datasets: we find it encouraging that our method is among those that passes this test here with each of the 31 SPMs.

2) *Finger-tapping experiments*: The next set of experiments involved the 12 replicated SPMs of [17] from the right-hand and left-hand finger tapping study of a right-hand-dominant male adult. Figure 10 displays the \mathcal{J} obtained for the 12 replications on each hand. For this experiment, we used $K_{\max} = 5$ and higher values of $\delta = 0.975, 0.985, 0.995$ to reflect our view that this is a motor experiment with few and very focused activation areas (and around 1-2% expected proportion of activated voxels). For the right-hand experiments, our method at $\delta = 0.975$ is marginally worse ($\mathcal{J} = 0.248$) than that obtained using CT ($\mathcal{J} = 0.252$) or pTFCE ($\mathcal{J} = 0.259$), however, our results obtained using $\delta = 0.985$ ($\mathcal{J} = 0.283$) and $\delta = 0.995$ ($\mathcal{J} = 0.308$) are substantially better than all competitors. For the left hand, we see that our method outperforms all its competitors. ([83] has expressed some concern about the

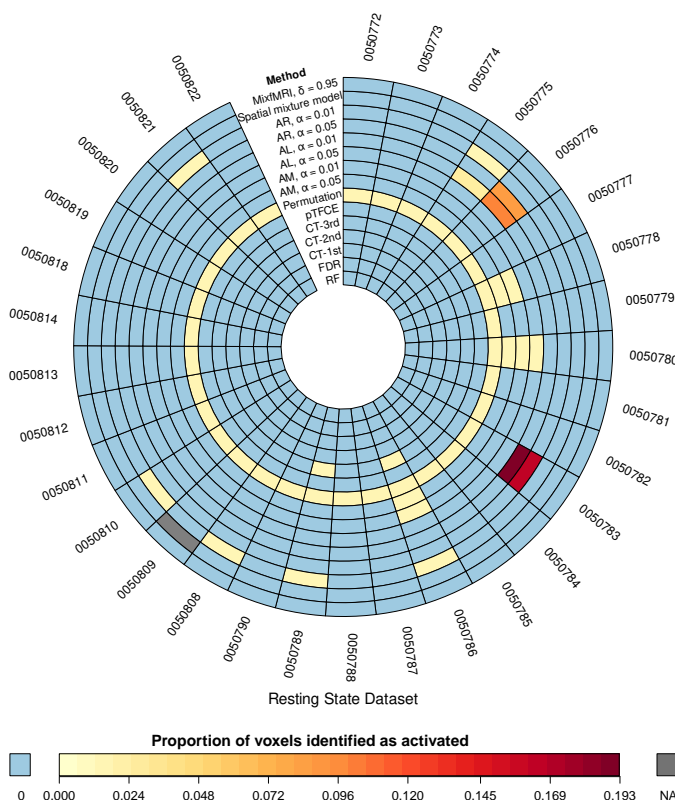


Fig. 9. The proportion of in-brain voxels identified by each of the competing methods as activated in each resting state dataset. Each dataset is indexed according to its seven-digit identifier. The greyed-out cell for the dataset “005089” reflects the inability of the spatial mixture model to decide on activation for this dataset, even after attempts with different parameter combinations.

quality of the data in the eighth left-hand experiment replicate, therefore we also evaluated \tilde{J} of the results after excluding this experiment. The \tilde{J} for almost all methods improve, but even here, MixfMRI is by far the best performer.) For these datasets, cluster thresholding does quite well, and is the next-best performer (after MixfMRI) in the left-hand experiments. The spatial mixture model approach performs modestly on these experiments, and is mildly to substantially (for the right-hand experiments) worse than FDR. AM-FAST, AR-FAST, ALL-FAST and permutation testing are, in that order, among the worse performers. An encouraging aspect of the \tilde{J} s for our method is its consistency in the right hand, that indicates that a higher restriction on δ identifies more similar areas of activation in each map. For the left-hand experiments, \tilde{J} goes up from $\delta = 0.975$ to $\delta = 0.985$, but dips slightly from there to $\delta = 0.995$, potentially attributed to the fact that this is a left-hand finger-tapping experiment performed by a right-hand dominant male. However, whether with the right or the left hand, our methodology is overall the better-performing method. We also comment that the generally low values of \tilde{J} for all methods provide support to concerns [41], [83] on potential issues in quality and preprocessing of this dataset.

3) *Flanker task experiments*: The Flanker task data are from a study [90] on 26 right-handed adults who were vi-

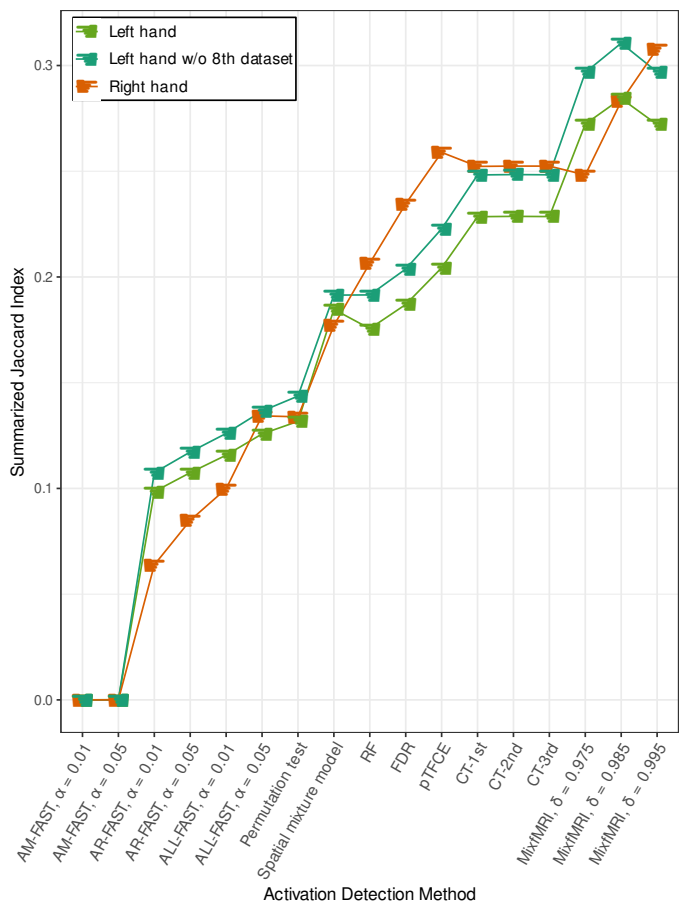


Fig. 10. The summarized Jaccard index (\tilde{J}) for assessing the similarity in the activation maps obtained by each method for the 12 right- and left-hand finger tapping experiments. Because of concerns [83], that the right-hand dominant male may have been tapping his right-hand fingers in the eighth dataset, \tilde{J} is also obtained for activation maps from the left-hand datasets sans the eighth replication.

cenarians or tricenarians, and were imaged using echoplanar imaging (TR=2000 ms, TE = 30 ms, flip angle = 80°) over 146 time-points to get, 146 $64 \times 64 \times 40$ image volumes of voxel size $3 \times 3 \times 4\text{mm}^3$, while participating in 12 congruent and 12 incongruent Eriksen flanker task trials, that were presented to them at varying intervals of 8 to 14 seconds, in pseudo-random order. We used AFNI to first preprocess the dataset to a common MNI template for each subject, and then fit a general linear model with the appropriate design matrix and first-order autoregressive moving average errors. From each dataset, we obtained a SPM that captured the contrast between the congruent and the incongruent task, and obtained the corresponding p -values at each voxel. This is an example of an experiment with a two-sided alternative hypothesis, and our method is applied using the additional development of Section III-F. Once again, there is no ground truth for comparison, but we note that although these SPMs are for different subjects, they are all of normal younger adults and in standardized space, and so we evaluate performance by calculating \tilde{J} between the activation (or significance) maps obtained on each SPM by each method. Here, the activation map specifies the significance or otherwise of a contrast, as determined by the applied

method. (Here, we evaluate **MixfMRI** with $K_{\max} = 11$, and using $\delta = 0.9, 0.95, 0.975$, with the higher values reflecting the circumstance that this is a two-sided hypothesis. Also, memory requirements in the **AnalyzefMRI** implementation of cluster thresholding precluded us from evaluating any of the CT-1st, CT-2nd, or CT-3rd methods so we do not include these methods in our comparisons.) Figure 11 summarizes the

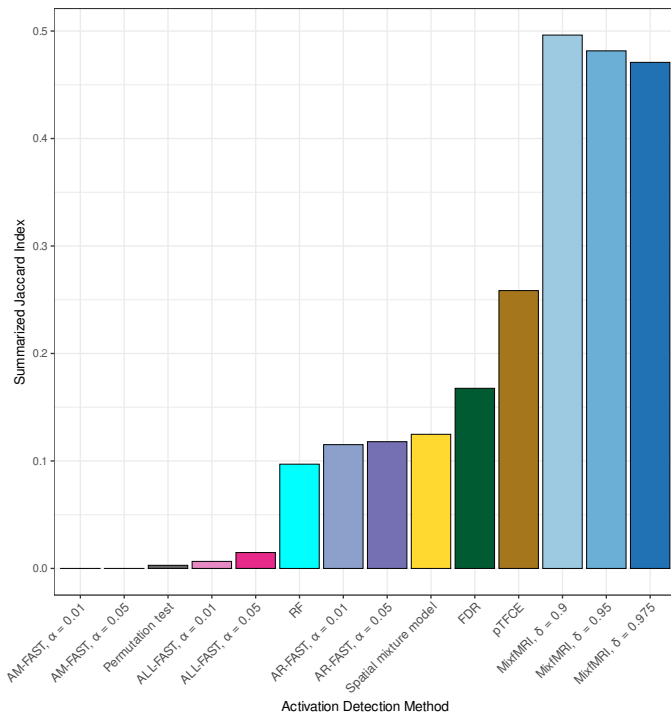


Fig. 11. The summarized Jaccard index for assessing the similarity in the significance maps obtained by each method for the 26 Flanker task experiments.

results and shows that our methods yield \tilde{J} -values that are almost twice as good as its closest competitor (pTFCE). The performance of FDR, spatial mixture model and the AR-FAST approaches is middling, while permutation testing and the other FAST methods perform poorly. It is unclear if the very marginal decrease in the consistency of the significance maps with increasing δ are themselves significant, but if so, may point to the difficulty of consistency identifying significance in higher-level tasks. However, we see that we are by far the best performer in this two-sided hypothesis testing scenario.

C. Summary of Results

The results of our experiments on both simulation and real data examples show good performance of our MixfMRI methodology developed in this paper. In both 2D and 3D simulation setups, our method is always a top performer. The superlative performance of the spatial mixture model in the 2D simulation experiments (for all but the highest model complexity) does not quite translate to the 3D simulation setup, and even more so, to the real-data 3D examples, where we are almost always the best method. Our method is also among those that correctly identify no activation in all 31 resting state datasets. Among the other methods, the second-best performer

is unclear in the 3D simulation experiments, but is pTFCE in the case of the finger-tapping and Flanker task real-life data experiments. Interestingly, and in general, the performance of permutation testing for detecting activation was anemic at best – a finding also reported in [41] and somewhat contrary to that of [35].

We close this section with a brief discussion on the specification of δ , the constraint on which is an integral part and major contribution of our work. Our simulation studies indicate that the choice of δ slightly affects performance for all three 2D phantoms and identification complexities, with greater relative (albeit marginal) inaccuracy when δ is misspecified downwards (*i.e.* δ is less than the true π_0) than with δ is specified to be greater than the true π_0 , where it still provides quite accurate identification. Given that it is impractical to expect a practitioner to precisely specify δ , it is encouraging to note the robustness of our method to the exact choice of δ .

V. ACTIVATION IN SPORTS IMAGINATION EXPERIMENT WITH IMPLICATIONS IN TREATMENT AND THERAPY OF PVS PATIENTS

We now re-analyze the sports imagination experiment dataset of Section II. Recall that the value of this experiment is in providing for a way to communicate with, and provide therapy and treatment for PVS patients [51], who because of TBI or other reasons, may have individualized brain structure and function that needs to be accurately identified. We therefore evaluate whether we can, as a follow-up to our very encouraging results of Section IV, accurately recover activation in a known normal subject where the results can be explained and interpreted against known cerebral structure and function, and where Section II has suggested unclear results with current standard analysis methods. We revisit this dataset by applying our refined methodology to the voxel-wise p -values obtained, as described in A-B. Here the most plausible value of δ is 0.99 but we also try $\delta = 0.975$ and 0.999 to check the effect of δ -misspecification. With $K_{\max} = 20$, BIC (and ICL-BIC) chose $\hat{K} = 11, 12$ and 6 for solutions using $\delta = 0.975, 0.99$ and 0.995. In either case, the inactive component did not merge with any of the other groups in the procedure outlined in the first part of Section III-D. Using the second part of Section III-D, the activated components merged to form four, five and four clusters with $\delta = 0.975, 0.99, 0.995$, respectively. We now discuss and interpret the results.

A. Analysis and interpretation of results

We focus our discussion on results obtained using $\delta = 0.99$. Figure 12 summarizes the results and indicates the five distinct regions identified as activated. We discuss these regions numbered (i) through (v), in decreasing order, of their averaged t -statistic (highlighted in Figure 12), recalling that the experimental paradigm is of a healthy female volunteer imaged alternately while at rest and while imagining playing tennis.

The region with the highest average (standardized) intensity of activation is among the smallest, and spans the calcarine

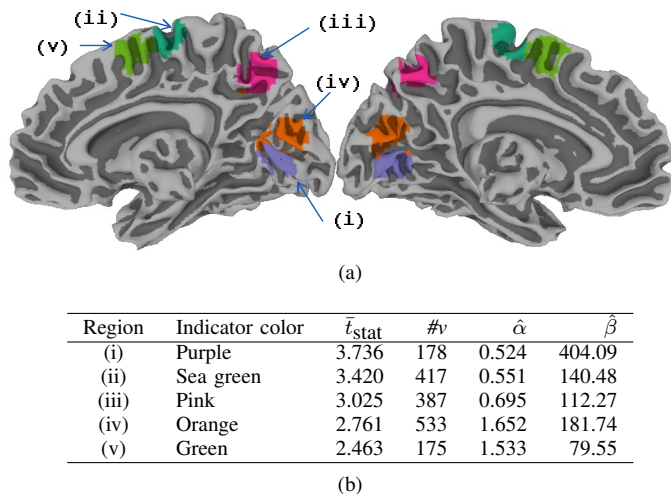


Fig. 12. (a) Activation detected using our method with $\delta = 0.99$ in a healthy female volunteer performing a sports imagination experiment. (b) The five activated regions, identified by their indicator color, the number of voxels ($\#v$), the average t statistic and estimated beta distribution parameters for each region. In that order, the five regions span (i) the calcarine sulcus and the inferior occipital cortex/lingual gyrus, (ii) the PMC, (iii) the pre-cuneus, (iv) the cuneus, and (v) the SMA.

sulcus and the inferior occipital cortex/lingual gyrus. The primary visual cortex – where dynamic and static information from the visual hemifields is organized coherently for later processing in the cuneus – is primarily located in the calcarine sulcus, while the inferior occipital/lingual gyrus is important for visual memory, attention, and in orienting the brain to visual location of an existing or remembered scene. That these regions would be activated with high intensity makes sense given that the subject is tasked with imagining playing tennis, and needs to recall visual imagery of the activity and in processing information in pretend-planning and executing her moves. But for the PVC which is identified rather faintly, these regions are not identified using cluster-wise thresholding, pTFCE (see Figure 1a, b) or many other methods.

The next highest average t -statistic is a large region in the primary motor cortex (PMC) that executes functions planned by the pre-motor areas. This area also includes a somatotopic map comparable to the somatosensory cortex, and has been associated with mental motor imagery and sensorimotor planning in multiple fMRI studies involving imagined movements [92]–[94]. Once again, the fact of these regions being activated makes sense in the context of the experimental paradigm, however, but for the tiny blip of activation in the somatosensory cortex, these regions were largely missed in cluster-wise thresholding or AR-FAST, and completely by methods other than pTFCE.

The region of activation with the third highest averaged t -statistic is in the precuneus which is an area of the brain that is known to be involved in the storage of long-term memory and in relating current and past experiences, self-reflection and cogitation. Given that the subject is tasked with imagining playing tennis that has to have her recollect and draw from her past experiences, it makes sense for the precuneus to show activation. The precuneus was also identified in the cluster-thresholding of Figure 1 but the spatial extent was low. This

region was also almost missed by pTFCE.

The fourth region is the largest activated region and spans the cuneus that is superjacent to the calcarine sulcus. This area is known to pre-process 3D space, color and other information while the next region includes the SMA that works in concert with the pre-SMA, the striatum, and other regions to collect prefrontally driven information about what the subject is doing and guides appropriate movement in space. This higher-order information is then sent to the PMC, which eventually directs motor movements. Once again, activation of these areas are in keeping with the experimental paradigm. Cluster-wise thresholding and pTFCE also identify this region, though the spatial extent of these regions is lower.

The fifth region is the smallest activated region and is mostly the Supplementary Motor Area (SMA). This region works in concert with pre-SMA, the striatum, and other regions to collect prefrontally driven information about what the organism is doing and where it should move in space to execute its goals. This higher order information is then sent to primary motor cortex, which eventually send movement commands to the limbs, face, and trunk. Once again, it is reasonable to expect activation in this region, considering the experimental paradigm, but AR-FAST, cluster thresholding and pTFCE miss this region entirely.

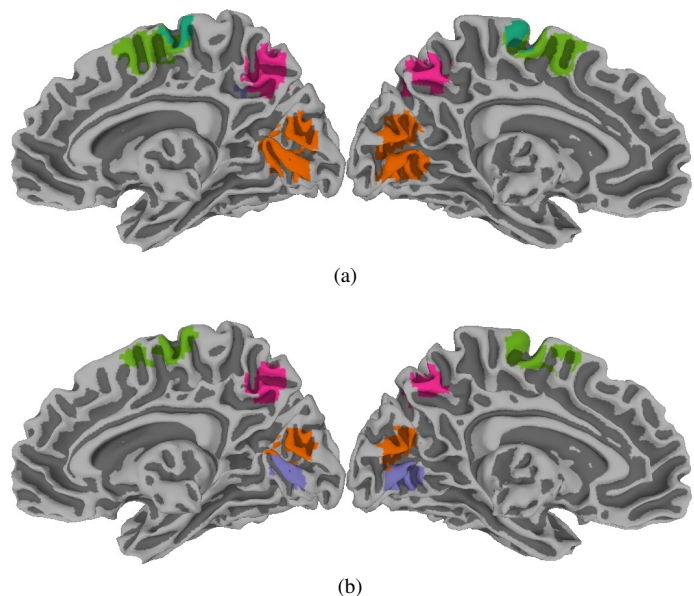


Fig. 13. Activation detected in a healthy female volunteer using our method with (a) $\delta = 0.975$ and (b) $\delta = 0.995$.

1) *Activation detection in sports imagination experiment with $\delta = 0.975$ and $\delta = 0.995$:* Figure 13 displays activation regions detected by our method with $\delta = 0.975$ and 0.995. Compared to Figure 12, both choices of δ result in one less region, but for different reasons. With $\delta = 0.975$, Figure 13a shows one less region than Fig 12, merging the cuneus with the calcarine sulcus and the inferior occipital cortex/lingual gyrus, while Figure 13b has the SMA and PMC placed in the same activated group. So the results are not very dissimilar and exhibit robustness with regard to modest misspecification of δ .

B. Significance of our findings

Our results with this imagination dataset indicate that our refinements that account for both spatial context and *a priori* constraints on the expected proportion of activated voxels can provide improved and interpretable activation detection in a single-subject sports imagination experiment. Specifically, when compared to the results from cluster-wise thresholding, pFTCE or AR-FAST (Figure 1) that only identified the first three of our regions and did not identify the cuneus which preprocesses information on 3D space and color, or the SMA that gathers prefrontal information to send to the PMC, our identified activation regions are clear and interpretable in the context of the experimental paradigm, providing confidence in our findings even though they are derived from a single subject. This demonstrated ability of our approach to identify these regions, each with different kinds of activation, is a major strength relative to all existing methods. This subject was a normal healthy female and so while her activation maps are interpretable in the context of the study, we would not *a priori* know this, for example with a TBI survivor or a patient in PVS, or more generally in a clinical setting. The original goal [51] of sports imagination experiments in patients in PVS was to facilitate therapy and provide ways of communication with them but, as explained in Section II, this benefit has not been realized because of murky activation detection even in group PVS patient experiments [53]. It is essential to have reliable activation detection at the individual subject level in order to permit therapy and communication with PVS patients and the development and analysis of this paper show promise in making this goal possible. More generally also, our refinements and improvements can improve activation detection at the individual level, making it possible to adopt fMRI in a clinical setting.

VI. DISCUSSION

We provide an improved activation detection approach in task-based fMRI that incorporates spatial context and also the proportion of voxels *a priori* expected to be activated as per the experimental paradigm. Our statistically sound model-based methodology is computationally practical and implemented in our **MixfMRI** R package. Simulation experiments on settings of low to very high detection difficulty indicated our methods to have superior performance over existing ones. Our methodology also correctly predicted no activation in null activation settings and was a top performer, in terms of consistency, or real-world datasets. When applied to a single-subject sports imagination experiment study, with deep implications in the treatment of PVS patients, the method provided interpretable results and improved activation detection, identifying regions that had not been activated by current methods. An additional benefit of our approach is the ability to differentiate intensities and kinds of activation. This augurs well for applying our methodology to clinical settings, such as with TBI survivors or subjects with impacted or individualized brains where accurate activation detection is essential to identify pathologies, treatments and therapy.

Our refinements are easily extended to situations beyond voxel-wise p -values of the SPM. For instance, our methodology could be easily extended to the SPM itself. Further, even in the context of p -values, we have developed our methodology using an approximate mixtures-of-beta mode, but we could easily incorporate more precise models, as for instance provided in [19]. Also, our methodology is really intended for single-subject studies, however, it can be easily adapted to apply to activation detection in multi-subject group studies. In this case, we simply apply our methodology to the SPM obtained from the group study. Activation detection could potentially be further improved by semi-supervised approaches that include known areas of inactivation, voxel-wise *a priori* activation probability maps drawn from normal subjects, or better processing such as including phase in the fMRI time-series data analysis [95]. Further, it may be worth investigating if the performance of competing methods, *e.g.*, the spatial mixture model, can be further improved by incorporating *a priori* constraints on the expected proportion of activated voxels. Thus, we see that while we have provided a substantial contribution to accurate activation detection in fMRI, a number of interesting extensions and investigations remain that may benefit from further attention.

ACKNOWLEDGEMENTS

The authors are very grateful to two anonymous reviewers whose comments on an earlier version of this manuscript greatly improved its content. Out sincere thanks also to B. Klinedinst and A. Willette of the Program in Neuroscience and the Department of Food Sciences and Human Nutrition at Iowa State University for help with the interpretation of Figure 12.

FUNDING

R. Maitra was supported in part by the National Institute of Biomedical Imaging and Bioengineering (NIBIB) of the National Institutes of Health (NIH) under Grant Nos. R21EB016212 and R21EB034184. The content of this paper is however solely the responsibility of the authors and does not represent the official views of the FDA, the NIBIB or the NIH.

DATA AVAILABILITY

The datasets used in the simulations is publicly available within the authors' R package **MixfMRI** implementing the methods. The sports imagination experiment dataset is publicly available at <https://www.jstatsoft.org/index.php/jss/article/downloadSuppFile/v044i11/v44i11-data.zip>. The processed SPM of p -values is available as the **pstats** object in the R package **MixfMRI**.

AVAILABILITY OF COMPUTER CODE

The methodology developed in this article is implemented in publicly available R package **MixfMRI** publicly available as a "Contributed package" at <https://www.r-project.org>. The latest developmental version of this package is available at <https://github.com/snoweye/MixfMRI>.

APPENDIX A
SPORTS IMAGINATION EXPERIMENT DATASET:
ADDITIONAL DETAILS

A. *Background*

The time-course sequence of images were acquired on a MR scanner using a gradient echo-echo planar imaging sequence with an echo time (TE) of 40 milliseconds, relaxation time (TR) of 2 seconds and an excitation flip angle of 80 degrees. At each time-point, the scanner acquired 30 axial slices of 4 mm thickness each and a field-of-view of 24 cm with an imaging grid of size 64×64 , yielding in-plane voxel dimensions of 3.75 mm. [53] do not provide detailed discussion and specific analysis of this dataset, but it was later used (without pre-processing) and publicly released by [54] to demonstrate features of their **fmri** software package in R [55].

B. *Data Preprocessing*

We used the umbrella `uber_subject.py` in the Analysis of Functional Neuroimaging (AFNI) software [58]–[60] to pre-process, register [96], [97] and analyze the dataset. The script consists of two main steps. First, the functional image data cube at all time points is registered with the anatomical data cube. Our registered and aligned 3D dataset had $46 \times 55 \times 43$ voxels, of which 33,753 voxels were inside the brain. There were 105 time-points with $TR=2s$, and the time series at each voxel was fit using the model

$$Y_t = \beta_0 + \beta_1 s_t + \beta_2 d_t + \beta_3 d_t^2 + \epsilon_t \quad (7)$$

where, at the t th time-point, Y_t is the observed BOLD response, s_t is the expected BOLD response obtained by convolving the input stimulus and the Hemodynamic Response Function (HRF), and d_t is the time drift parameter (that is assumed to have a quadratic effect on the observed BOLD response), and ϵ_t is the noise or error in the observation with an assumed autoregressive moving average ARMA(1,1) dependence structure. (Here, we have temporarily dropped the subscript for the voxel for readability but it is present in all the parameters and the random quantities in (7).) Our voxel-specific parameters allow us to account for local inhomogeneities – the voxel-wise fitting of the model is also computationally practical. At this stage, we do not account for any spatial structure in the model. Although all parameters are fit, our interest in this experiment is only in knowing if the parameter β_1 is positive or not. Framed in terms of a hypothesis testing problem, we test $H_0 : \beta_1 = 0$ v.s. $H_a : \beta_1 > 0$ at each voxel which means that there is a positive association between the observed BOLD response at that voxel and the expected BOLD response after accounting for other factors. All other parameters are nuisance parameters and of no primary importance. At each voxel, we test $H_0 : \beta_1 = 0$ against $H_a : \beta_1 > 0$ which means that there is a significant voxel response to stimulus when H_0 is rejected. Thus, the t -statistics for testing the hypothesis of no activation against the alternative of positive association with the expected BOLD response are obtained at each voxel.

Because our analysis outlined above does not account for spatial context, the t -statistics were spatially smoothed for

consistency using the automated robust method of [91] which uses generalized cross-validation to adaptively estimate the smoothing parameter. The p -value of activation at each voxel was computed at each voxel from these test statistics. These obtained p -values were used to construct activation maps.

C. *Constructing Activation Maps*

The p -values at each voxel were thresholded to construct activation maps using some common approaches. These maps and the test-statistics at those voxels were then mapped using the SURface MAPPING tool (SUMA) of [98]. We used FDR with $q = 0.05$ [12], [56] and found no activation, highlighting the challenges faced by a global thresholding method such as controlling FDR for constructing activation maps for experiments such as this one. We also used cluster-wise thresholding methods to detect activation with AFNI's 3dClustSim package to determine the minimum number of contiguous voxels in each activation region at a threshold of 0.001 (following [31]) using first-, second- and third-order neighborhoods.

APPENDIX B
STATISTICAL METHODOLOGY: ADDITIONAL DETAILS

A. *Parameter Estimation via The EM Algorithm*

1) *Proof of Result 1:* Define the Lagrangian $\mathcal{L}(\boldsymbol{\pi}, \lambda_e, \lambda_l) = g(\boldsymbol{\pi}; \mathbf{W}) - \lambda_e h_e(\boldsymbol{\pi}) - \lambda_l h_l(\boldsymbol{\pi})$ with convex set $\boldsymbol{\Pi}$. Then $\boldsymbol{\pi}^*$ is a local maximum if and only if there exists exactly one λ_l^* satisfying stationarity (*i.e.* having $\nabla_{\boldsymbol{\pi}} \mathcal{L}(\boldsymbol{\pi}^*, \lambda_e^*, \lambda_l^*) = 0$) and the Karush-Kuhn-Tucker (KKT) conditions [68]. Note that the constraint functions $h_e(\boldsymbol{\pi})$ and $h_l(\boldsymbol{\pi})$ are both affine, so all KKT conditions are satisfied.

The stationarity condition for maximizing $g(\boldsymbol{\pi}; \mathbf{W})$ yields $\boldsymbol{\pi}^*$ satisfying the equations:

$$-\frac{1}{\pi_k^*} \sum_{i=1}^n w_{ik} + \lambda_e^* + \lambda_l^* 1_{(k=0)} = 0, \quad \text{for } k = 0, 1, \dots, K. \quad (8)$$

The inequality constraint is inactive if $\lambda_l^* = 0$. This means that the local minimizer $\boldsymbol{\pi}^*$ of $g(\boldsymbol{\pi}; \mathbf{W})$ under the equality constraint ($h_e(\boldsymbol{\pi}) = 0$) is a feasible solution for our problem. We now consider the case of the active inequality constraint, that is, $\lambda_l^* > 0$, for which we use the KKT conditions. Primal feasibility is itself defined by the constraint in (b). The dual feasibility condition stipulates that $\lambda_l^* \geq 0$ so with an active inequality constraint it is enough to focus on $\lambda_l^* > 0$. Combining this condition ($\lambda_l^* > 0$) with complementary slackness ($\lambda_l^* h_l(\boldsymbol{\pi}^*) > 0$) yields $\pi_0^* = \delta$. From (8) we get $\pi_k^* = \sum_{i=1}^n w_{ik} / \lambda_e^*$ for each $k = 1, 2, \dots, K$. From the constraint (a), we have $\pi_0^* + \sum_{i=1}^K \pi_k^* = 1$ so that $\sum_{i=1}^K \pi_k^* = 1 - \delta$ under the active equality constraint. Thus, we get $\lambda_e^* = \sum_{k=1}^K \sum_{i=1}^n w_{ik} / (1 - \delta)$ from where we get $\pi_k^* = (1 - \delta) \sum_{i=1}^n w_{ik} / \sum_{k=1}^K \sum_{i=1}^n w_{ik} = (1 - \delta) \pi_k^* / (1 - \pi_0^*)$ for $k = 1, 2, \dots, K$. The result follows upon combining the cases with active and inactive inequality constraints. \square

2) *Initialization and Classification*: The *Rnd-EM* approach [19] chooses – from a pre-set number M ($M = 50$ in this paper) of “valid” randomly-realized initial values Θ^* – the configuration maximizing (5) and uses that to initialize EM which is then run till convergence. We now discuss the issue of choosing the initializing random realizations. We choose each random initializer one component at a time. Specifically, we let $(0.5, \bar{\mathbf{v}}^\top)^\top$ be the initializing center for the first (inactivated) component, where $\bar{\mathbf{v}}$ represents the coordinates of the central voxel in the image volume and the choice of 0.5 is from the mean of the uniform distribution. For the initializing parameters of the beta distributions of the activated components, we randomly select K other values from among the p -values of voxels of potential interest, for example, from voxels whose p -values were below some p_{\max} (say 0.05). The coordinates from each of these K voxels are our initializers for these K μ_k 's.

We now group each voxel in terms of the closest Euclidean distance of the observed $(p_i, \mathbf{v}_i^\top)^\top$ to the potential initializing candidates. (Note that the voxel coordinates \mathbf{v} 's are scaled to lie in $[0, 1]$, so that all voxel coordinates and p -values are of comparable importance in the Euclidean distance for grouping. For each group k , comprising the initially assigned p -values and voxel coordinates $(p_{jk}, \mathbf{v}_{jk}^\top)^\top; j = 1, 2, \dots, n_k$, we set $\pi_k = n_k/n$ to be the proportion of voxels assigned to the k th group and the remaining components of Θ_k from the maximizer of the log-density $\sum_{j=1}^{n_k} \log[b(p_{jk}; \alpha_k, \beta_k) \phi(\mathbf{v}_{jk}; \mu_k, \Sigma_k)]$ under constraints (ii) and (iii).

We declare a candidate initializer “invalid” when a random initial grouping yields a single observation in some group, resulting in a degenerate initial Σ_k for that group. (Invalid candidates are discarded from further consideration.) We select the best initial value as $\Theta^{(0)} = \arg\max_{\Theta^*} \ell(\Theta^*; \mathbf{p}, \mathbf{v})$ from which the EM algorithm of the constrained mixture model is applied. We consider a MLE valid if the EM algorithm of **B-A** converges to non-degenerate parameter estimates and leads to non-degenerate groups (*i.e.*, each cluster has at least a few observations, say $1 + c_v$). The converged result from the best initial value does not always lead to a valid MLE, so we repeat the *Rnd-EM* approach until we get a valid MLE. From the converged valid MLE $\hat{\Theta}$, we estimate \hat{w}_{ik} the *maximum a posteriori* (MAP) evaluated at $\hat{\Theta}$ and classify the i th voxel to the l th component where $l = \arg\max_k \hat{w}_{ik}$.

3) *Parallelizing EM for use with fMRI data*: Let our APECMa algorithm for maximizing (5) consist of the $C = K + 1$ cycles given by $\mathbb{C} = \{\{\pi, \Gamma_0\}, \{\pi, \Gamma_1\}, \dots, \{\pi, \Gamma_K\}\}$ with each cycle containing a CM-step followed by a partial E-step (PE). For example, PE-steps only update $u_{i,c}^{(s+[c]C)} \equiv f_c(p_i, \mathbf{v}_i; |\Gamma_c^{(s+[c]C)})$ for the c th cycle of the iteration s where $c = 0, 1, 2, \dots, C - 1$. The extra space here is $((u_{ik}))_{1 \leq i \leq n; 0 \leq k \leq K}$ corresponding to the $((w_{ik}))_{1 \leq i \leq n; 0 \leq k \leq K}$. There is no need to update components other than the c th component because $u_{ik}^{(s+[c]C)} \equiv u_{ik}^{(s+1)}$ for $k < c$ have been updated in a previous cycle of the same iteration s , while $u_{ik}^{(s+[c]C)} = u_{ik}^{(s)}$ for $k > c$ have not changed

from the previous iterated value at $\Gamma_k^{(s+[k]C)}$. Therefore,

$$w_{ik}^{(s+[c]C)} = \frac{\pi_k^{(s+[c]C)} u_{i,c}^{(s+[c]C)}}{\sum_{k=0}^K \pi_k^{(s+[c]C)} u_{i,k}^{(s+[c]C)}}$$

for all i and k , completing the E-step for the c th cycle of the s th iteration. The CM-steps are performed in turn on the c th cycle and utilize $w_{ik}^{(s+[c]C)}$ in the same manner as the M-step of the EM algorithm, but restricted to $\{\pi, \Gamma_c\}$ for the c th cycle.

The EGM algorithm requires no further changes to the PE-steps, since we may distribute the dataset $\mathbf{X}_{n \times (1+c_v)} \equiv ((p_i, \mathbf{v}_i^\top)_{i,j})_{1 \leq i \leq n; 1 \leq j \leq (1+c_v)}$ in consecutive row blocks into D cores for the EGM algorithm. For example, each core contains one row block of the dataset, say $\mathbf{X}_{n_d \times (1+c_v)}$, with n_d observations in the d th core and $\sum_{d=1}^D n_d = n$. ($n_d \approx n/D$ is ideally for gaining computation performance.) Similarly, we distribute w_{ik} 's and u_{ik} 's into the D cores with dimensions $n_d \times (K + 1)$. Therefore, the PE-steps in the data-distributed computed environment are the same as in the serial environment and no communication across cores is needed. Moreover, each core needs less computation – about $1/D$ on the average – for the EGM algorithm.

The CM-steps, however, need adjustment for application of the EGM algorithm. For the mixing proportion, the unconstrained estimates are

$$\pi_{k^*}^{(s+[c]C)} = \frac{\sum_{d=1}^D \sum_{i=1}^{n_d} w_{i,k}^{(s+[c]C)}}{\sum_{j=1}^K \sum_{d=1}^D \sum_{i=1}^{n_d} w_{i,j}^{(s+[c]C)}}$$

where $\sum_{i=1}^{n_d} w_{i,j}^{(s+[c]C)}$ is the sufficient statistics calculated locally for each d core and is gathered/reduced in the G-step from all the other $(D - 1)$ cores. The constrained estimates for $\pi_k^{(s+[c]C)}$ can be adjusted accordingly. Unlike Γ_k 's, π is involved in every cycle so that all π_k 's need to be updated in each cycle in order to fulfill conditions that guarantee validity of the EM steps, such as monotonicity of the log likelihood and space-filling of the parameter space [71]. For the beta distribution parameters with constraints, we numerically optimize the objective function (in terms of α_c and β_c for $c > 0$) required by the `constrOptim()` function in R, such that $\sum_{i=1}^{n_d} w_{i,c}^{(s+[c]C)} \log b(p_i; \alpha_c, \beta_c)$ is maximized under the constraint (iii) where $\sum_{i=1}^{n_d} w_{i,c}^{(s+[c]C)} \log b(p_i; \alpha_c, \beta_c)$ are the sufficient statistics of the objective function calculated locally given each new numerical update of (α_c, β_c) . For the normal components, we compute

$$\mu_c^{(s+[c]C)} = \sum_{d=1}^D \sum_{i=1}^{n_d} w_{i,c}^{(s+[c]C)} \mathbf{v}_i / \sum_{d=1}^D \sum_{i=1}^{n_d} w_{i,c}^{(s+[c]C)}$$

and $\Sigma_c^{(s+[c]C)}$ which is the diagonal matrix containing the diagonal elements of

$$\frac{\sum_{d=1}^D \sum_{i=1}^{n_d} w_{i,c}^{(s+[c]C)} (\mathbf{v}_i - \mu_c^{(s+[c]C)}) (\mathbf{v}_i - \mu_c^{(s+[c]C)})^\top}{\sum_{d=1}^D \sum_{i=1}^{n_d} w_{i,c}^{(s+[c]C)}}$$

where $\sum_{i=1}^{n_d} w_{i,c}^{(s+[c]C)} \mathbf{v}_i$, $\sum_{i=1}^{n_d} w_{i,c}^{(s+[c]C)}$, and $\sum_{i=1}^{n_d} w_{i,c}^{(s+[c]C)} (\mathbf{v}_i - \mu_c^{(s+[c]C)}) (\mathbf{v}_i - \mu_c^{(s+[c]C)})^\top$ are the sufficient statistics for the G-step.

APPENDIX C

PERFORMANCE EVALUATIONS: ADDITIONAL DETAILS

A. Illustrative examples to show the effect of the identification complexity parameter

We first provide sample illustrations (Figures 14, 15, and 16) of the generative mechanism used to simulate the p -values in our 2D simulation. The identification complexity parameter ω controls the difficulty and the specificity of the activation problem and we display sample densities, realizations and detected activation images for representative $\omega = 0.01, 0.5, 0.75$. Thus, the difficulty of our activation detection problem in our sample illustrations spans from the moderately easy to the very difficult. As explained in Section IV-A1, the p -values are realizations from one of k densities given by $\psi(p; \nu_k) = \phi(\Phi_z^{-1}(1-p); \nu_k, 1) / \phi_z(\Phi_z^{-1}(1-p))$. Note that $\nu_0 = 0$ and at that value, the density reduces to the standard uniform density (corresponding to the distribution of p -values from the inactivated component). π_0, π_1 and π_2 are set to be the proportion of pixels in each region for the given kind of phantom. With these π_0, π_1 and π_2 , and ν_1 and ν_2 are chosen to satisfy $\omega_{kl} = \omega$ for all $k \neq l \in \{0, 1, 2\}$, where ω_{kl} is the overlap measure as defined in [73]. The left panels of Figures 14, 15, and 16 show sample densities obtained for $\omega = 0.01, 0.5, 0.75$. Simulated p -values are then realized from $\psi(p; \nu_k)$. Sample SPMs obtained from realizations of p -values obtained from each of the realized densities in Figures 14, 15 and 16 are also displayed (in terms of values, atop each density figure) and as the first image in the right panels.

B. Illustrative example of performance in simulation settings

The other images in the right panels of Figures 14, 15, and 16 display, for each setting, and in order, activation images obtained using our competitors (using values, where appropriate, parameter values that yielded the better performance).

REFERENCES

- [1] J. W. Belliveau, D. N. Kennedy, R. C. McKinstry, B. R. Buchbinder, R. M. Weisskoff, M. S. Cohen, J. M. Vevea, T. J. Brady, and B. R. Rosen, "Functional mapping of the human visual cortex by magnetic resonance imaging," *Science*, vol. 254, pp. 716–719, 1991.
- [2] K. K. Kwong, J. W. Belliveau, D. A. Chesler, I. E. Goldberg, R. M. Weisskoff, B. P. Poncelet, D. N. Kennedy, B. E. Hoppel, M. S. Cohen, R. Turner, H.-M. Cheng, T. J. Brady, and B. R. Rosen, "Dynamic magnetic resonance imaging of human brain activity during primary sensory stimulation," *Proceedings of the National Academy of Sciences*, vol. 89, pp. 5675–5679, 1992.
- [3] P. A. Bandettini, A. Jesmanowicz, E. C. Wong, and J. S. Hyde, "Processing strategies for time-course data sets in functional MRI of the human brain," *Magnetic Resonance in Medicine*, vol. 30, pp. 161–173, 1993.
- [4] A. M. Howsemann and R. W. Bowtell, "Functional magnetic resonance imaging: imaging techniques and contrast mechanisms," *Philosophical Transactions of the Royal Society, London*, vol. 354, pp. 1179–94, 1999.
- [5] M. A. Lindquist, "The statistical analysis of fMRI data," *Statistical Science*, vol. 23, no. 4, pp. 439–464, 2008.
- [6] N. A. Lazar, *The Statistical Analysis of Functional MRI Data*. Springer, 2008.
- [7] S. Ogawa, T. M. Lee, A. S. Nayak, and P. Glynn, "Oxygenation-sensitive contrast in magnetic resonance image of rodent brain at high magnetic fields," *Magnetic Resonance in Medicine*, vol. 14, pp. 68–78, 1990.
- [8] S. Ogawa, T. M. Lee, A. R. Kay, and D. W. Tank, "Brain magnetic resonance imaging with contrast dependent on blood oxygenation," *Proceedings of the National Academy of Sciences*, vol. 87, no. 24, pp. 9868–9872, 1990.
- [9] K. J. Friston, A. P. Holmes, K. J. Worsley, J.-B. Poline, C. D. Frith, and R. S. J. Frackowiak, "Statistical parametric maps in functional imaging: A general linear approach," *Human Brain Mapping*, vol. 2, pp. 189–210, 1995.
- [10] K. J. Friston, C. D. Frith, P. F. Liddle, R. J. Dolan, A. A. Lammertsma, and R. S. J. Frackowiak, "The relationship between global and local changes in PET scans," *Journal of Cerebral Blood Flow and Metabolism*, vol. 10, pp. 458–466, 1990.
- [11] K. J. Worsley, S. Marrett, P. Neelin, A. C. Vandal, K. J. Friston, and A. C. Evans, "A unified statistical approach for determining significant voxels in images of cerebral activation," *Human Brain Mapping*, vol. 4, pp. 58–73, 1996.
- [12] C. R. Genovese, N. A. Lazar, and T. Nichols, "Thresholding of statistical maps in functional neuroimaging using the false discovery rate," *Neuroimage*, vol. 15, pp. 870–878, 2002.
- [13] B. R. Logan and D. B. Rowe, "An evaluation of thresholding techniques in fMRI analysis," *NeuroImage*, vol. 22, pp. 95–108, 2004.
- [14] M. M. Monti, "Statistical analysis of fMRI time-series: A critical review of the GLM approach," *Frontiers in Human Neuroscience*, vol. 5, no. 00028, pp. 1–13, 2011. [Online]. Available: http://www.frontiersin.org/Journal/Abstract.aspx?s=537&name=human_neuroscience&ART_DOI=10.3389/fnhum.2011.00028
- [15] B. Biswal, A. E. DeYoe, and J. S. Hyde, "Reduction of physiological fluctuations in fMRI using digital filters," *Magnetic Resonance in Medicine*, vol. 35, no. 1, pp. 107–113, January 1996. [Online]. Available: <http://view.ncbi.nlm.nih.gov/pubmed/8771028>
- [16] J. V. Hajnal, R. Myers, A. Oatridge, J. E. Schweiso, J. R. Young, and G. M. Bydder, "Artifacts due to stimulus-correlated motion in functional imaging of the brain," *Magnetic Resonance in Medicine*, vol. 31, pp. 283–291, 1994.
- [17] R. Maitra, S. R. Roys, and R. P. Gullapalli, "Test-retest reliability estimation of functional MRI data," *Magnetic Resonance in Medicine*, vol. 48, pp. 62–70, 2002.
- [18] R. P. Gullapalli, R. Maitra, S. Roys, G. Smith, G. Alon, and J. Greenspan, "Reliability estimation of grouped functional imaging data using penalized maximum likelihood," *Magnetic Resonance in Medicine*, vol. 53, pp. 1126–1134, 2005.
- [19] R. Maitra, "Assessing certainty of activation or inactivation in test-retest fMRI studies," *Neuroimage*, vol. 47, pp. 88–97, 2009.
- [20] T. E. Nichols and S. Hayasaka, "Controlling the familywise error rate in functional neuroimaging: a comparative review," *Statistical Methods in Medical Research*, vol. 12, pp. 419–446, 2003.
- [21] Y. Benjamini and R. Heller, "False discovery rates for spatial signals," *Journal of the American Statistical Association*, vol. 102, no. 480, pp. 1272–1281, 2007.
- [22] —, "Screening for partial conjunction hypotheses," *Biometrics*, vol. 64, pp. 1215–1222, 2008.
- [23] K. J. Friston, C. Frith, P. Liddle, and R. Frackowiak, "Comparing functional (pet) images: the assessment of significant change," *Journal of Cerebral Blood Flow and Metabolism*, vol. 11, no. 4, p. 690, 1991.
- [24] K. J. Worsley, A. C. Evans, S. Marrett, and P. Neelin, "A three-dimensional statistical analysis for CBF activation studies in human brain," *Journal of Cerebral Blood Flow and Metabolism*, vol. 12, no. 6, p. 900–918, 1992.
- [25] K. J. Worsley, "Local maxima and the expected Euler characteristic of excursion sets of χ^2 , F and t fields," *Advances in Applied Probability*, vol. 26, pp. 13–42, 1994.
- [26] K. J. Worsley and J. E. Taylor, "An improved theoretical p value for SPMs based on discrete local maxima," *NeuroImage*, vol. 28, p. 1056–1062, 2005.
- [27] R. Adler, *The geometry of random fields*. New York: Wiley, 1981.
- [28] K. J. Friston, P. Zeigler, and R. Turner, "Analysis of functional MRI time-series," *Human Brain Mapping*, vol. 1, pp. 153–171, 1994.
- [29] S. Hayasaka and T. E. Nichols, "Validating cluster size inference: random field and permutation methods," *Neuroimage*, vol. 20, p. 2343–2356, 2003.
- [30] S. Forman, J. Cohen, M. Fitzgerald, W. Eddy, M. Mintun, and D. Noll, "Improved assessment of significant activation in functional magnetic resonance imaging (fMRI): use of a cluster-size threshold," *Magnetic Resonance in Medicine*, vol. 33, p. 636–647, 1995.
- [31] C.-W. Woo, A. Krishnan, and T. D. Wager, "Cluster-extent based thresholding in fMRI analyses: Pitfalls and recommendations," *Neuroimage*, vol. 91, p. 412–419, 2014.
- [32] S. M. Smith and T. E. Nichols, "Threshold-free cluster enhancement: Addressing problems of smoothing, threshold dependence and localisation in cluster inference," *Neuroimage*, vol. 44, pp. 83–98, 2009.

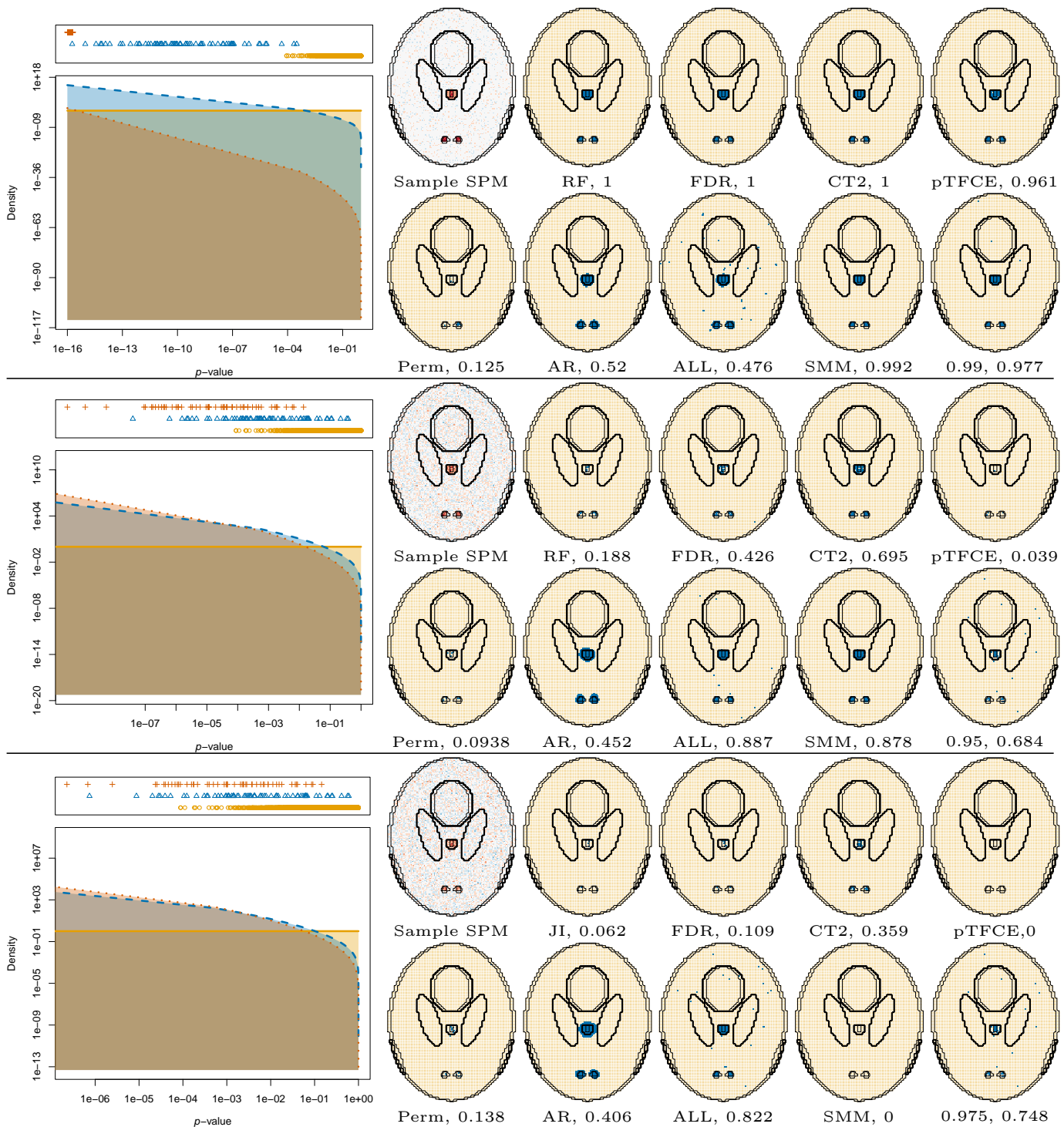


Fig. 14. Sample realizations and activation detection for identification complexity $\omega = 0.01$ (top set), $\omega = 0.50$ (middle set) and $\omega = 0.75$ (bottom set) on simulations obtained using the phantom in Figure 3a. For each set of values, we have, in the left panel, a density of p -values, including a realization (placed atop the density plots) of p -values using the generative model for $\pi_0 = 0.977$. The right panel displays a (i) sample SPM, obtained by calculating the upper quantile of the simulated p -values, as well as activation maps (along with their \mathcal{J}) obtained using (ii) RF, (iii) FDR, (iv) CT-2nd, (v) pTFCE, (vi) permutation testing (Perm in the figure), (vii) AR-FAST, with $\alpha = 0.01$, (viii) ALL-FAST, with $\alpha = 0.01$, (ix) SMM, and (x) MfnoX, with the best-performing δ from among $\{0.95, 0.975, 0.99\}$, and the choice indicated by the first value in the legend.

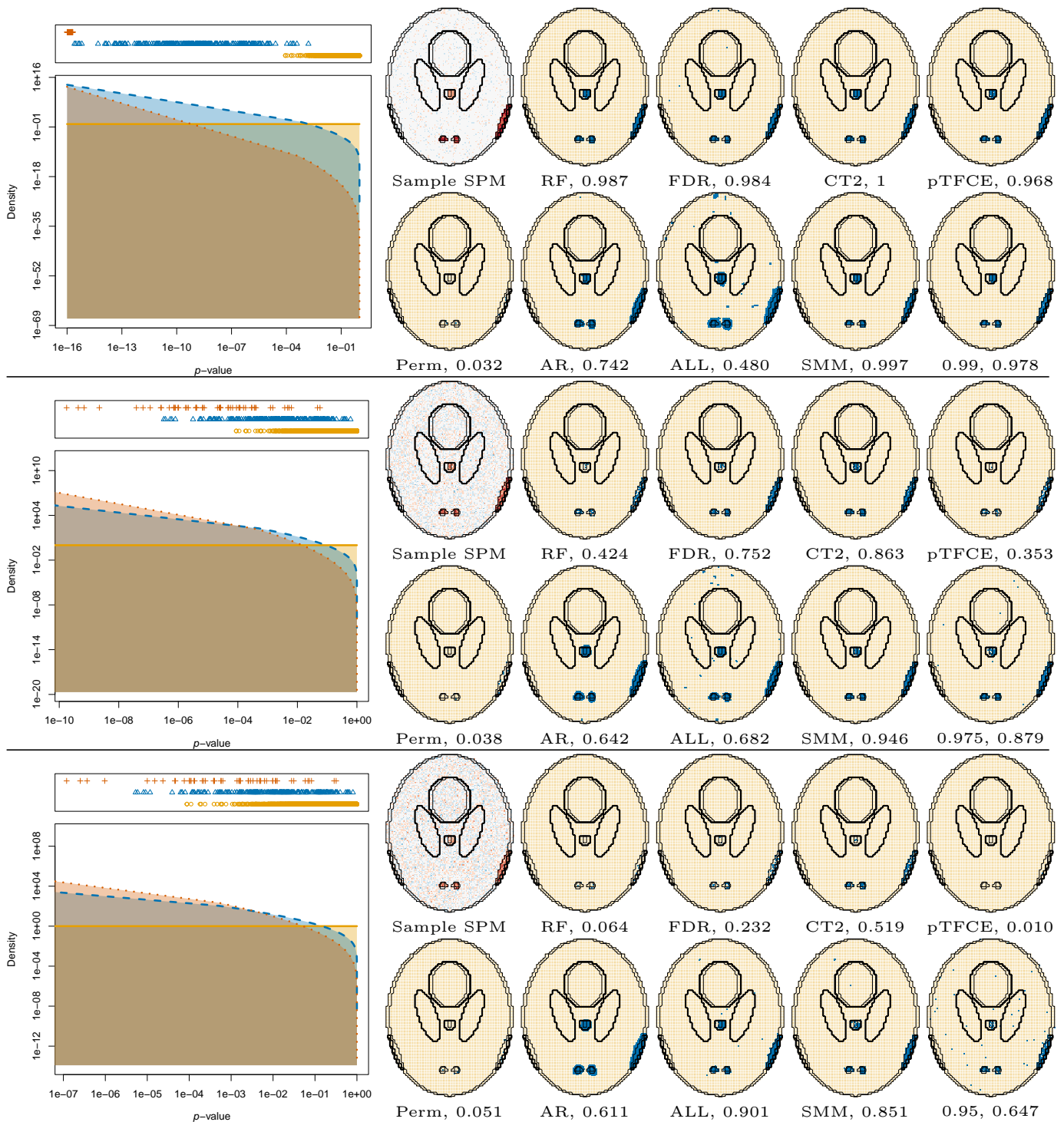


Fig. 15. Sample realizations and activation detection for identification complexity $\omega = 0.01$ (top set), $\omega = 0.50$ (middle set) and $\omega = 0.75$ (bottom set) on simulations obtained using the phantom in Figure 3b. For each set of values, we have, in the left panel, a density of p -values, including a realization (placed atop the density plots) of p -values using the generative model for $\pi_0 = 0.977$. The right panel displays a (i) sample SPM, obtained by calculating the upper quantile of the simulated p -values, as well as activation maps (along with their \mathcal{J}) obtained using (ii) RF, (iii) FDR, (iv) CT-2nd, (v) pTFCE, (vi) permutation testing (Perm in the figure), (vii) AR-FAST, with $\alpha = 0.01$, (viii) ALL-FAST, with $\alpha = 0.01$, (ix) SMM, and (x) MfnoX, with the best-performing δ from among $\{0.95, 0.975, 0.99\}$, and the choice indicated by the first value in the legend.

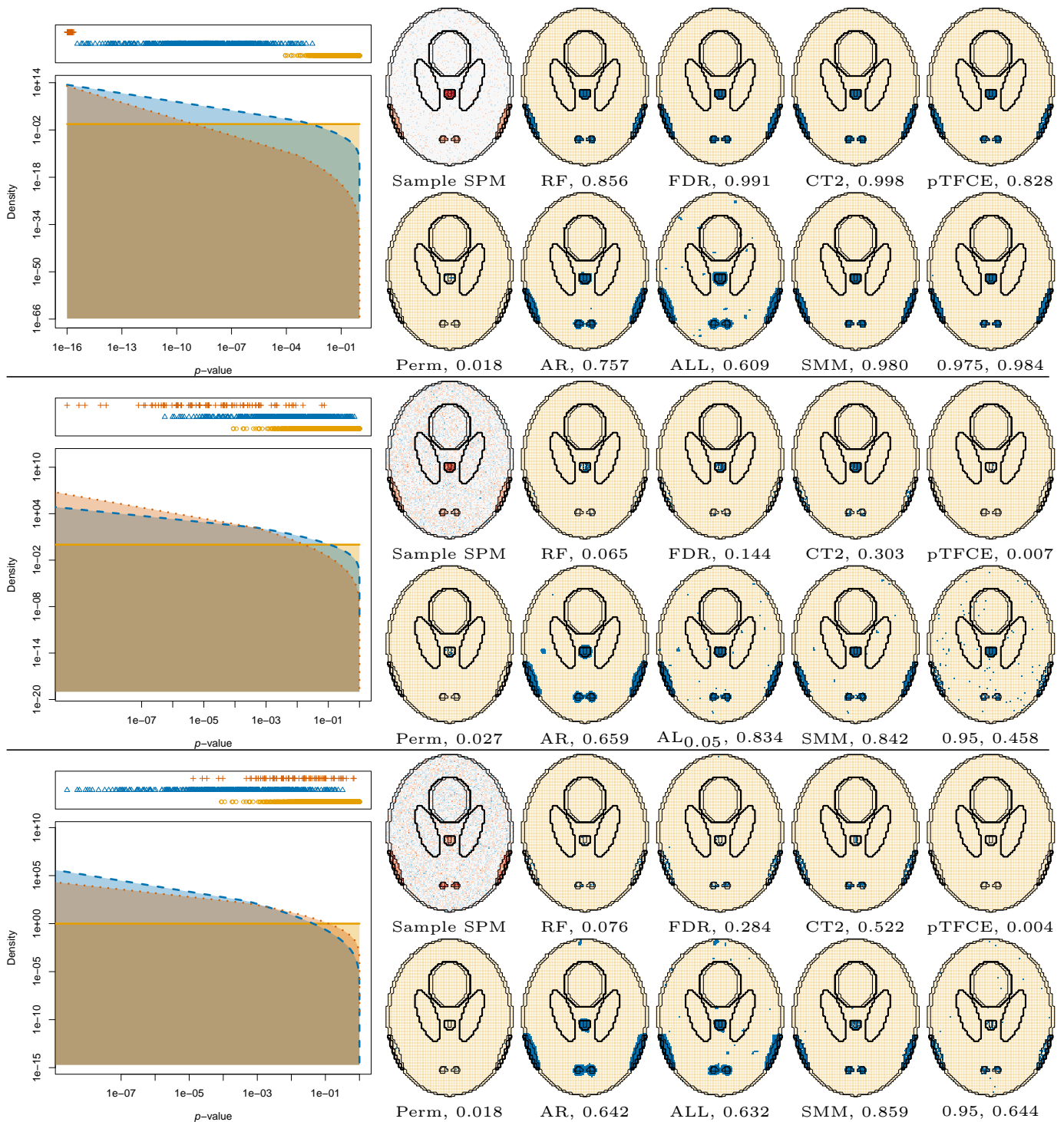


Fig. 16. Sample realizations and activation detection for identification complexity $\omega = 0.01$ (top set), $\omega = 0.50$ (middle set) and $\omega = 0.75$ (bottom set) on simulations obtained using the phantom in Figure 3c. For each set of values, we have, in the left panel, a density of p -values, including a realization (placed atop the density plots) of p -values using the generative model for $\pi_0 = 0.977$. The right panel displays a (i) sample SPM, obtained by calculating the upper quantile of the simulated p -values, as well as activation maps (along with their \mathcal{J}) obtained using (ii) RF, (iii) FDR, (iv) CT-2nd, (v) pTFCE, (vi) permutation testing (Perm in the figure), (vii) AR-FAST, with $\alpha = 0.01$, (viii) ALL-FAST, with $\alpha = 0.01$, (ix) SMM, and (x) MfoX, with the best-performing δ from among $\{0.95, 0.975, 0.99\}$, and the choice indicated by the first value in the legend.

- [33] R. Heller, D. Stanley, D. Yekutieli, N. Rubin, and Y. Benjamini, "Cluster-based analysis of fMRI data," *NeuroImage*, vol. 33, no. 2, pp. 599–608, Nov. 2006. [Online]. Available: <http://dx.doi.org/10.1016/j.neuroimage.2006.04.233>
- [34] T. Spisák, Z. Spisák, M. Zunhammer, U. Bingel, S. Smith, T. Nichols, and T. Kincses, "Probabilistic TFCE: A generalized combination of cluster size and voxel intensity to increase statistical power," *NeuroImage*, vol. 185, pp. 12–26, 2019.
- [35] A. Eklund, T. Nichols, M. Andersson, and H. Knutsson, "Empirically investigating the statistical validity of SPM, FSL and AFNI for single subject fMRI analysis," in *IEEE International symposium on biomedical imaging (ISBI)*, 2015, p. 1376–1380.
- [36] A. Eklund, T. E. Nichols, and H. Knutson, "Correction for Eklund et al., cluster failure: Why fMRI inferences for spatial extent have inflated false-positive rates," *Proceedings of the National Academy of Sciences*, vol. 113, no. 33, pp. E4929–E4929, 2016. [Online]. Available: <http://www.pnas.org/content/113/33/E4929>
- [37] D. Kessler, M. Angststadt, and C. S. Sripada, "Reevaluating "cluster failure" in fMRI using nonparametric control of the false discovery rate," *Proceedings of the National Academy of Sciences*, vol. 114, no. 17, pp. E3372–E3373, 2017. [Online]. Available: <http://www.pnas.org/content/114/17/E3372>
- [38] R. W. Cox, G. Chen, D. R. Glen, R. C. Reynolds, and P. A. Taylor, "fMRI clustering and false-positive rates," *Proceedings of the National Academy of Sciences*, vol. 114, no. 17, pp. E3370–E3371, 2017. [Online]. Available: <http://www.pnas.org/content/114/17/E3370>
- [39] Brain Research through Advancing Innovative Neurotechnologies (BRAIN) Working Group Report to the Advisory Committee to the Director, NIH, "BRAIN 2025: A SCIENTIFIC VISION," 2014.
- [40] E. N. Brown and M. Behrmann, "Controversy in statistical analysis of functional magnetic resonance imaging data," *Proceedings of the National Academy of Sciences*, vol. 114, no. 17, pp. E3368–E3369, 2017. [Online]. Available: <http://www.pnas.org/content/114/17/E3368>
- [41] I. A. Almodóvar-Rivera and R. Maitra, "FAST adaptive smoothed thresholding for improved activation detection in low-signal fMRI," *IEEE Transactions on Medical Imaging*, vol. 38, no. 12, pp. 2821–2828, 2019.
- [42] N. V. Hartvig and J. L. Jensen, "Spatial mixture modeling of fMRI data," *Human Brain Mapping*, vol. 11, no. 4, pp. 233–248, 2000. [Online]. Available: [http://dx.doi.org/10.1002/1097-0193\(200012\)11:4<233::AID-HBM10>3.0.CO;2-F](http://dx.doi.org/10.1002/1097-0193(200012)11:4<233::AID-HBM10>3.0.CO;2-F)
- [43] C. R. Genovese, "A Bayesian time-course model for functional Magnetic Resonance Imaging data (with discussion)," *Journal of the American Statistical Association*, vol. 95, no. 451, pp. 691–719, 2000.
- [44] M. Smith and L. Fahrmeir, "Spatial bayesian variable selection with application to functional magnetic resonance imaging," *Journal of the American Statistical Association*, vol. 102, no. 478, pp. 417–431, 2007. [Online]. Available: <http://pubs.amstat.org/doi/abs/10.1198/01621450600001031>
- [45] K. Friston, W. Penny, C. Phillips, S. Kiebel, G. Hinton, and J. Ashburner, "Classical and bayesian inference in neuroimaging: Theory," *NeuroImage*, vol. 16, no. 2, pp. 465–483, 2002. [Online]. Available: <https://www.sciencedirect.com/science/article/pii/S1053811902910906>
- [46] K. Friston, D. Glaser, R. Henson, S. Kiebel, C. Phillips, and J. Ashburner, "Classical and bayesian inference in neuroimaging: Applications," *NeuroImage*, vol. 16, no. 2, pp. 484–512, 2002. [Online]. Available: <https://www.sciencedirect.com/science/article/pii/S1053811902910918>
- [47] F. D. Bowman, B. Caffo, S. S. Bassett, and C. Kilts, "A bayesian hierarchical framework for spatial modeling of fmri data," *NeuroImage*, vol. 39, no. 1, pp. 146–156, 2008. [Online]. Available: <https://www.sciencedirect.com/science/article/pii/S1053811907007306>
- [48] W.-Y. Ahn, A. Krawitz, W. Kim, J. R. Busemeyer, and J. W. Brown, "A model-based fmri analysis with hierarchical bayesian parameter estimation," *Journal of Neuroscience, Psychology, and Economics*, vol. 4, no. 2, p. 95–110, 2011.
- [49] The Multi-Society Task Force on PVS, "Medical aspects of the persistent vegetative state," *New England Journal of Medicine*, vol. 330, pp. 1499–1508, 1994.
- [50] N. D. Schiff, U. Ribary, D. R. Moreno, B. Beattie, E. Kronberg, R. Blasberg, J. Giacino, C. McCagg, J. J. Fins, R. Llinás, and F. Plum, "Residual cerebral activity and behavioural fragments can remain in the persistently vegetative brain," *Brain*, vol. 125, no. 6, pp. 1210–1234, 2002.
- [51] A. M. Owen, M. R. Coleman, M. Boly, M. H. Davis, S. Laureys, and J. D. Pickard, "Detecting awareness in the vegetative state," *Science*, vol. 313, no. 5792, p. 1402, 2006.
- [52] M. M. Monti, A. Vanhaudenhuyse, M. R. Coleman, M. Boly, J. D. Pickard, L. Tshibanda, A. M. Owen, and S. Laureys, "Willful modulation of brain activity in disorders of consciousness," *New England Journal of Medicine*, vol. 362, no. 7, p. 579–89, 2010.
- [53] J. C. Bardin, J. J. Fins, D. I. Katz, J. Hersh, L. A. Heier, K. Tabelow, J. P. Dyke, D. J. Ballon, N. D. Schiff, and H. U. Voss, "Dissociations between behavioural and functional magnetic resonance imaging-based evaluations of cognitive function after brain injury," *Brain*, vol. 134, pp. 769–782, 2011.
- [54] K. Tabelow and J. Polzehl, "Statistical parametric maps for functional MRI experiments in R: The package fmri," *Journal of Statistical Software*, vol. 44, no. 11, pp. 1–21, 10 2011. [Online]. Available: <http://www.jstatsoft.org/v44/i11>
- [55] R Core Team, *R: A Language and Environment for Statistical Computing*, R Foundation for Statistical Computing, Vienna, Austria, 2018. [Online]. Available: <http://www.R-project.org/>
- [56] Y. Benjamini and D. Yekutieli, "The control of the false discovery rate in multiple testing under dependency," *The Annals of Statistics*, vol. 29, no. 4, pp. 1165–1188, 2001. [Online]. Available: <http://www.jstor.org/stable/2674075>
- [57] A. M. Winkler, G. R. Ridgway, M. A. Webster, S. M. Smith, and T. E. Nichols, "Permutation inference for the general linear model," *NeuroImage*, vol. 92, pp. 381–397, 2014.
- [58] R. W. Cox, "AFNI: software for analysis and visualization of functional magnetic resonance neuroimages," *Computers and biomedical research, an international journal*, vol. 29, no. 3, pp. 162–173, 1996.
- [59] R. W. Cox and J. S. Hyde, "Software tools for analysis and visualization of fMRI data," *NMR in Biomedicine*, vol. 10, no. 4-5, pp. 171–178, 1997.
- [60] R. W. Cox, "AFNI: What a long strange trip it has been," *NeuroImage*, vol. 62, pp. 743–747, 2012.
- [61] R. A. Parker and R. B. Rothenberg, "Identifying important results from multiple statistical tests," *Statistics in Medicine*, vol. 7, pp. 1031–1043, 1988.
- [62] D. B. Allison, G. L. Gadbury, M. Heo, J. R. Fernández, C.-K. Les, J. A. Prolla, and R. Weindruch, "A mixture model approach for the analysis of microarray gene expression data," *Computational Statistics and Data Analysis*, vol. 39, pp. 1–20, 2002.
- [63] S. Pounds and S. W. Morris, "Estimating the occurrence of false positives and false negatives in microarray studies by approximating and partitioning the empirical distribution of p -values," *Bioninformatics*, vol. 19, pp. 1236–1242, 2003.
- [64] A. P. Dempster, N. M. Laird, and D. B. Rubin, "Maximum likelihood for incomplete data via the EM algorithm (with discussion)," *Journal of the Royal Statistical Society, Series B*, vol. 39, pp. 1–38, 1977.
- [65] G. J. McLachlan and T. Krishnan, *The EM Algorithm and Extensions*. Wiley, 2008.
- [66] K. Lange, *Numerical Analysis for Statisticians*. Springer-Verlag, 2010.
- [67] C. Wu, "On the convergence properties of the EM algorithm," *Annals of Statistics*, vol. 11, pp. 95–103, 1983.
- [68] S. Boyd and L. Vandenberghe, *Convex Optimization*. Cambridge: Cambridge University Press, 2004.
- [69] X. Meng and D. van Dyk, "The EM algorithm — an old folk-song sung to a fast new tune (with discussion)," *Journal of the Royal Statistical Society B*, vol. 59, pp. 511–567, 1997.
- [70] W.-C. Chen and R. Maitra, "Model-based clustering of regression time series data via APECM — an AECM algorithm sung to an even faster beat," *Statistical Analysis and Data Mining*, vol. 4, no. 6, pp. 567–578, 2011. [Online]. Available: <http://dx.doi.org/10.1002/sam.10143>
- [71] W.-C. Chen, G. Ostrouchov, D. Pugmire, M. Prabhat, and M. Wehner, "A parallel em algorithm for model-based clustering with application to explore large spatio-temporal data," *Technometrics*, vol. 55, pp. 513–523, 2013.
- [72] R. Maitra, "Initializing partition-optimization algorithms," *IEEE/ACM Transactions on Computational Biology and Bioinformatics*, vol. 6, pp. 144–157, 2009.
- [73] R. Maitra and V. Melnykov, "Simulating data to study performance of finite mixture modeling and clustering algorithms," *Journal of Computational and Graphical Statistics*, vol. 19, no. 2, pp. 354–376, 2010.
- [74] V. Melnykov and R. Maitra, "Finite mixture models and model-based clustering," *Statistics Surveys*, vol. 4, pp. 80–116, 2010.
- [75] H. Akaike, "Information theory and an extension of the maximum likelihood principle," in *Selected Papers of Hirotugu Akaike*. Springer, 1973, pp. 199–213.
- [76] G. Schwarz, "Estimating the dimensions of a model," *Annals of Statistics*, vol. 6, pp. 461–464, 1978.
- [77] R. E. Kass and A. E. Raftery, "Bayes factors," *Journal of the American Statistical Association*, vol. 90, no. 430, pp. 773–795, 1995.

- [78] Y. Benjamini and Y. Hochberg, "Controlling the false discovery rate: A practical and powerful approach to multiple testing," *Journal of the Royal Statistical Society. Series B (Methodological)*, vol. 57, no. 1, pp. 289–300, 1995. [Online]. Available: <http://dx.doi.org/10.2307/2346101>
- [79] J. Polzehl, H. U. Voss, and K. Tabelow, "Structural adaptive segmentation for statistical parametric mapping," *NeuroImage*, vol. 52, no. 2, pp. 515–523, 2010.
- [80] W.-C. Chen and R. Maitra, "MixfMRI: fMRI clustering analysis," 2017, r Package, <http://cran.r-project.org/package=MixfMRI>.
- [81] C. Bordier, M. Dojat, and P. L. de Micheaux, "Temporal and spatial independent component analysis for fMRI data sets embedded in the AnalyzeFMRI R package," *Journal of Statistical Software*, vol. 44, no. 9, pp. 1–24, 2011. [Online]. Available: <http://www.jstatsoft.org/v44/i09/>
- [82] P. Jaccard, "Étude comparative de la distribution florale dans une portion des alpes et des jura," *Bulletin del la Société Vaudoise des Sciences Naturelles*, vol. 37, p. 547–579, 1901.
- [83] R. Maitra, "A re-defined and generalized percent-overlap-of-activation measure for studies of fMRI reproducibility and its use in identifying outlier activation maps," *Neuroimage*, vol. 50, pp. 124–135, 2010.
- [84] L. Hubert and P. Arabie, "Comparing partitions," *Journal of classification*, vol. 2, no. 1, pp. 193–218, 1985.
- [85] Y. Vardi, L. A. Shepp, and L. A. Kaufman, "Statistical model for Positron Emission Tomography," *Journal of the American Statistical Association*, vol. 80, pp. 8–37, 1985.
- [86] R. Maitra and F. O'Sullivan, "Variability assessment in Positron Emission Tomography and related generalized deconvolution models," *Journal of the American Statistical Association*, vol. 93, pp. 1340–1355, 1998.
- [87] M. Welvaert, J. Durnez, B. Moerkerke, G. Verdoolaege, and Y. Rosseel, "neuRosim: An R package for generating fMRI data," *Journal of Statistical Software*, vol. 44, no. 10, pp. 1–18, 2011. [Online]. Available: <http://www.jstatsoft.org/v44/i10/>
- [88] R. Henson, T. Shallice, M. Gorno-Tempini, and R. Dolan, "Face Repetition Effects in Implicit and Explicit Memory Tests as Measured by fMRI," *Cerebral Cortex*, vol. 12, no. 2, pp. 178–186, 02 2002.
- [89] M. B. Nebel, S. Joel, J. Muschelli, A. Barber, B. Caffo, J. Pekar, and S. Mostofsky, "Disruption of functional organization within the primary motor cortex in children with autism," *Human Brain Mapping*, vol. 35, pp. 567–580, 02 2014.
- [90] A. C. Kelly, L. Q. Uddin, B. B. Biswal, F. X. Castellanos, and M. P. Milham, "Competition between functional brain networks mediates behavioral variability," *NeuroImage*, vol. 39, no. 1, pp. 527–537, 2008.
- [91] D. Garcia, "Robust smoothing of gridded data in one and higher dimensions with missing values," *Computational Statistics and Data Analysis*, vol. 54, pp. 1167–1178, 2010.
- [92] M. Roth, J. Decety, M. Raybaudi, R. Massarelli, C. Delon-Martin, C. Segabarth, S. Morand, A. Gemignani, M. Decorps, and M. Jeannerod, "Possible involvement of primary motor cortex in mentally stimulated movement: a functional magnetic resonance imaging study," *NeuroReport*, vol. 7, p. 1280–1284, 1996.
- [93] M. Lotze, P. Montoya, M. Erb, E. Hülsmann, H. Flor, U. Klose, N. Birbaumer, and W. Grodd, "Activation of cortical and cerebellar motor areas during executed and imagined hand movements: a functional MRI study," *Journal of Cognitive Neuroscience*, vol. 11, p. 491–501, 1999.
- [94] C. Stippich, H. Ochmann, and K. Sartor, "Somatotopic mapping of the human primary sensorimotor cortex during motor imagery and motor execution by functional magnetic resonance imaging," *Neuroscience Letters*, vol. 331, p. 50–54, 2002.
- [95] D. W. Adrian, R. Maitra, and D. B. Rowe, "Complex-valued time series modeling for improved activation detection in fMRI studies," *Annals of Applied Statistics*, vol. 12, no. 3, pp. 1451–1478, 2018.
- [96] R. W. Cox and A. Jesmanowicz, "Real-time 3d image registration for function MRI," *Magnetic Resonance in Medicine*, vol. 42, pp. 1014–1018, 1999.
- [97] Z. S. Saad, D. R. Glen, G. Chen, M. S. Beauchamp, R. Desai, and R. W. Cox, "A new method for improving functional-to-structural mri alignment using local pearson correlation," *NeuroImage*, vol. 44, pp. 839–848, 2009.
- [98] Z. S. Saad and R. C. Reynolds, "SUMA," *NeuroImage*, vol. 62, pp. 767–772, 2012.